nature communications

Article

https://doi.org/10.1038/s41467-025-58392-3

Dynamic in-situ reconstruction of active site circulators for photo-Fenton-like reactions

Received: 29 May 2024

Accepted: 20 March 2025

Published online: 28 March 2025

Check for updates

Chang-Wei Bai[1,3], Fu-Qiao Yang[1,3], Pi-Jun Duan[1,3], Zhi-Quan Zhang[1], Yi-Jiao Sun[1], Xin-Jia Chen[1], Fei Chen[1] ✉ & Han-Qing Yu[2] ✉

Developing efficient and stable heterogeneous catalysts for the continuous activation of oxidants is crucial to mitigating the global water resource crisis. Guided by computational predictions, this research achieved this goal through the synthesis of a modified graphitic carbon nitride with enhanced catalytic activity and stability. Its intrinsic activity was further amplified by dynamic in-situ reconstruction using the I^-/I_3^- redox mediator system during photoreactions. Impressively, this reconstructed catalyst demonstrated the capability for at least 30 regeneration cycles while maintaining high purification efficacy. The mechanism underlying the in-situ reconstruction of active sites for periodate functionalization was elucidated through theoretical calculations, coupled with *semi*-in-situ X-ray photoelectron spectroscopy (XPS) and electrochemical analyses. The system's capacity to detoxify recalcitrant pollutants was demonstrated through successful *Escherichia coli* cultivation and Zebrafish embryo experiments. The economic feasibility and environmental impacts are quantitatively assessed by the Electrical Energy per Order (EE/O) metric and Life Cycle Assessment (LCA), confirming the system's scalability and applicability in real-world scenarios. This *dual-site* constrained interlayer insertion, and controllable in-situ catalyst reconstruction achieve durable robustness of the photocatalyst, paving the way for the development of sustainable catalytic water purification technologies.

The development of an ideal Fenton-like system that utilizes visible light to activate oxidants for the degradation and mineralization of organic pollutants offers an efficient and sustainable method for wastewater purification[1,2]. Despite its potential, several challenges impede its widespread adoption, including the incomplete oxidation of organic micropollutants, the reduction in activity due to the loss of active species, and practical difficulties in scaling the technology for industrial applications[3,4]. A pivotal strategy to address these issues involves enhancing the sustained generation of potent oxidants throughout the activation process, necessitating the design of efficient and stable photocatalysts[5,6]. In this regard, graphitic carbon nitride (g-C_3N_4, or CN) is a promising material, favored for its environmental compatibility, straightforward synthesis, and appropriate band structure conducive to photo-Fenton-like reactions[7,8]. Nevertheless, the intrinsic low mobility of photo-generated carriers in bulk CN curtails its overall photocatalytic efficacy[9,10].

To mitigate these limitations, numerous strategies, including crystalline modification, molecular engineering, formation of hetero/homojunctions, defect introduction, and doping, have been systematically investigated to amplify CN's performance[11–15]. Ion intercalation is particularly impactful, profoundly affecting CN's physical attributes, surface states, and electronic structure, thereby optimizing catalytic

[1]Key Laboratory of the Three Gorges Reservoir Region's Eco-Environment, Ministry of Education, College of Environment and Ecology, Chongqing University, Chongqing, China. [2]CAS Key Laboratory of Urban Pollutant Conversion, Department of Environmental Science and Engineering, University of Science and Technology of China, Hefei, China. [3]These authors contributed equally: Chang-Wei Bai, Fu-Qiao Yang, Pi-Jun Duan. ✉e-mail: fchen0505@cqu.edu.cn; hqyu@ustc.edu.cn

active sites and facilitating photo-generated carrier mobility[16]. The embedding of alkali metals, such as K^+ or Na^+, has been notably successful in enhancing light absorption and charge separation efficiency by introducing new energy levels[17,18]. This tactic has garnered considerable interest for applications in H_2 storage, H_2O_2 production, and CO_2 reduction[19–21]. The integration of non-metal elements like B, O, S, or I can also adjust CN's band structure and intrinsic electronic properties, enhancing conductivity, narrowing the band gap, and boosting light capture capabilities[22]. A strategy combining metal and non-metal modifications could significantly boost in-plane charge transfer in CN, thus enhancing its photocatalytic activity[23]. However, while in-plane doping can bolster charge transfer within CN layers, it contributes minimally to charge transfer between layers, which is vital for fully realizing CN's intrinsic activity[24]. Achieving synergistic activation of oxidants by simultaneously introducing targeted elements into both the CN plane and interlayers through dual-site constrained interlayers is challenging. This complexity stems from the sensitivity of the doping process to reaction conditions, precursors, and the low thermal stability during CN synthesis, highlighting the need for innovative approaches in catalyst design.

The catalytic activity and stability of the chosen catalyst are critical for effectively deploying photo-Fenton-like systems. While many photocatalysts exhibit robust initial activity, their performance frequently declines after extended use due to diminished photo-generated carrier separation and photo-corrosion[25,26]. A primary challenge arises when the rate of photo-generated charge transfer exceeds that of surface water oxidation, leading to an accumulation of photo-generated holes. This accumulation typically leads to surface charge carrier recombination and subsequent photo-corrosion of the catalyst[27]. Therefore, there is an urgent requirement to develop superior modification strategies that enhance both the migration rates of photo-generated carriers and their effective utilization. Addressing these elements is crucial for concurrently advancing and maintaining the balance between catalytic activity and stability.

Furthermore, the long-term operation of photocatalysts can alter their composition and structure, a process known as dynamic catalyst reconstruction[28,29]. This in-situ process is pivotal for improving the photo-stability of catalysts, as it often leads to the generation of new active species that significantly influence the binding strength between the catalyst and reactants, thereby affecting the rate of catalytic reactions[30]. Historically, the dynamic reconstruction of catalysts in photo-Fenton-like systems has been poorly understood. Additionally, assessments of catalyst reconstruction phenomena have varied. Some studies have identified in-situ catalyst reconstruction as a primary cause of catalyst deactivatio[31,32], whereas others argue that catalysts undergoing reconstruction form the "real catalytic centers" essential for the target reaction, suggesting that prior to reconstruction, these catalysts function merely as "pre-catalysts"[33,34]. Therefore, a profound understanding of catalyst reconstruction mechanisms and their effective modulation is crucial. Such knowledge will facilitate the development of catalysts that not only exhibit high activity but also maintain robust photo-stability, thereby advancing the field of photocatalytic water treatment.

Recent studies have highlighted the pivotal role of redox mediators, specifically I^-/I_3^-, which serve as intermediate electron carriers or reservoirs in the development of advanced charge transfer energy storage systems[35]. The dynamic cycling of these I^-/I_3^- redox mediators has been demonstrated to improve reaction kinetics and continuously neutralize high oxidation state species, resulting in batteries characterized by high surface capacity and extended lifespans of up to 2600 h[36,37]. Inspired by these findings, the integration of precise dual-site constrained interlayer insertion strategies with innovative in-situ reconstruction of I^-/I_3^- redox mediators offers significant potential for enhancing both the activity and stability of modified CN in photo-activated oxidant systems. A notable challenge and an opportunity arises from the inherent photo-stability limitations of potassium iodide (KI), where abundant I^- is susceptible to oxidation to I_3^-. Exploiting this behavior, I^-/I_3^- redox mediators can be introduced in situ during photocatalytic reactions to facilitate catalyst reconstruction and achieve dual-site constrained insertion between CN layers. This method represents a strategic approach for designing innovative functional catalysts. Cycling I^-/I_3^- redox mediators through catalyst reconstruction not only boosts the migration of photo-generated charge carriers but also efficiently consumes unreacted holes, thereby preventing surface recombination and reducing photo-corrosion. Additionally, this cycling temporarily stores photo-generated electrons, which are not immediately utilized in reactions and releases them in subsequent cycles to sustain reaction continuity.

Within this innovative framework, modified CN featuring dual-site constrained interlayer insertion functions as a "pre-catalyst" paired with the potent oxidant periodate (PI, IO_4^-), known for its high oxidation potential (+1.6 eV) and cost-effective storage and transport[38,39]. This photo-Fenton-like system is designed to exploit the advantages of in-situ redox mediator introduction during photocatalytic reactions, thereby maximizing the catalytic activity and stability of modified CN. This innovative paradigm synchronously optimizes both activity and stability through structural refinements, heralding a transformative shift in catalyst design. Comprehending the structure-activity relationships amid dynamic structural adjustments and their influence on the catalytic activity and stability of these systems is paramount. This understanding has profound implications for enhancing robust Fenton-like reactions and offers a meaningful trajectory for future research and development.

In this work, we synthesize a modified CN with K^+ and I^- intercalation (CN-KI), using a recrystallized mixture of melamine and KI. This precursor is further adapted to generate I_3^- in situ ($3I^- - 2e^- \rightarrow I_3^-$) during a photo-activated periodate (PI) process, enabling the dynamic reconstruction of the photocatalyst with the I^-/I_3^- redox mediator (CN-KI-I_3) (Fig. 1a). Our research focuses on the degradation of the antibiotic sulfamethoxazole (SMX), conducting an extensive investigation into the photocatalytic activity of the CN-KI-PI system under various parameters. Additional studies explore the stability of the CN-KI-I_3/PI system through detailed theoretical analyses and a series of *semi*-in-situ characterizations, aiming to elucidate the mechanisms behind the in-situ formation of the I^-/I_3^- redox mediator and the enhancements in stability they confer. Furthermore, the activation, role, and functionality of PI within this strategically designed system are rigorously evaluated. The system's sustainability and environmental impact are also thoroughly assessed, with toxicity levels tested from bacterial, plant, and animal perspectives through experiments involving *Escherichia coli* and Zebrafish embryo. Moreover, the application potential of CN-KI-I_3/PI system is demonstrated in various scenarios using continuous flow reactors and pilot-scale setups, underscoring its scalability and practical utility. A comprehensive Life Cycle Assessment (LCA) and Electrical Energy per Order (EE/O) analysis are conducted to evaluate the environmental and economic impacts of the CN-KI-I_3/PI system during real wastewater treatment, re-assessing the potential for industrial application of the designed system. This work sheds light on the dynamic reconstruction of redox mediators within the catalyst and their operational mechanisms in catalytic reactions. It also aims to optimize the balance between activity and stability. Ultimately, the goal is to broaden the applicability of photocatalytic technologies for organic wastewater purification.

Results and discussion

Computational prediction of constrained site insertion and in-situ catalyst reconfiguration

Advanced computational simulations elucidated the enhancement of the intrinsic properties of in-situ catalyst reconfiguration, underscoring the crucial role of polyiodinated species intercalation into

https://doi.org/10.1038/s41467-025-58392-3

carbon nitride (CN) during photoreaction. Initially, four distinct model systems were conceptualized: bulk CN, CN with K^+ and I^- insertion (CN-KI), CN with K^+ and I_3^- insertion (CN-KI_3), and CN with K^+, I^-/I_3^- redox constrained interlayer insertion (CN-KI-I_3). These models underwent optimization via preliminary theoretical calculations (Supplementary Fig. 1) to assess the feasibility of in-situ CN reconstruction using I^-/I_3^- redox mediators and to evaluate the impact and functionality of potassium and various iodine species within the CN interlayers. Electrostatic potentials and two-dimensional charge density maps were generated to illustrate the electron cloud distribution across these

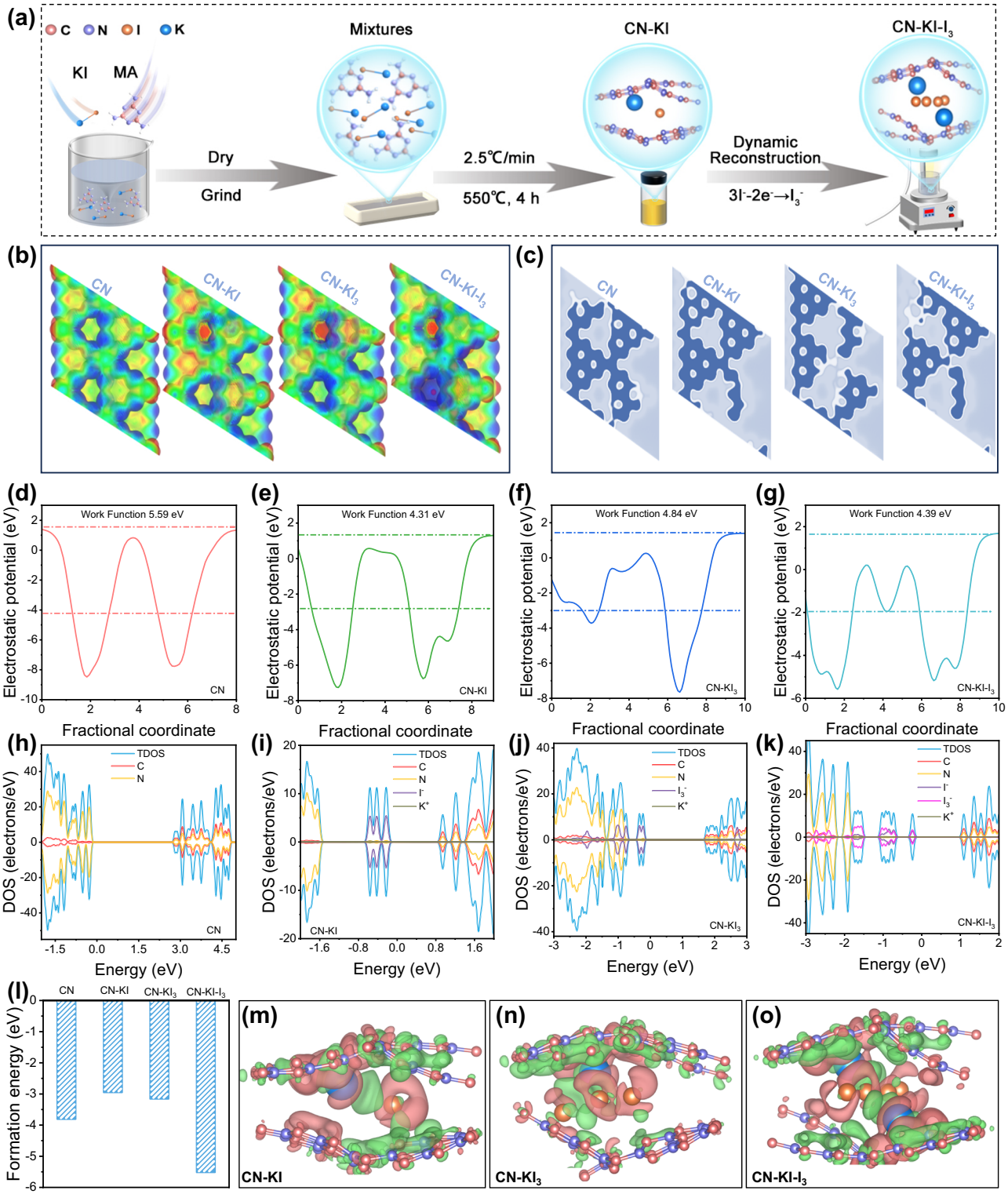

Fig. 1 | Insights into constrained interlayer insertion and catalyst restructuring potential. a Schematic representations of different catalyst synthesis methods. Electrostatic potential maps (**b**) and two-dimensional electron density profiles (**c**) for each catalyst variant. **d**–**g** Surface work functions for CN, CN-KI, CN-KI_3, and CN-KI-I_3. **h**–**k** Electronic state densities for each catalyst. **l** Comparative formation energies for different catalysts. **m**–**o** Electron density difference diagrams for CN-KI, CN-KI_3, and CN-KI-I_3.

systems (Fig. 1b, c). The highly symmetric structure of bulk CN resulted in a uniform distribution of electron-deficient and electron-rich regions, correlating with its lackluster catalytic performance due to restricted carrier migration. In contrast, the CN-KI and CN-KI_3 configurations demonstrated that the strong electronegativity of I^- or I_3^- shifted electron clouds from the center of the heptazine ring to these ions, disrupting the original uniform charge distribution and creating new negative electron-rich regions. This modification significantly enhanced photo-generated carrier migration and intrinsic photocatalytic activity. Moreover, in the CN-KI-I_3 system, where both I^- and I_3^- were simultaneously introduced, the charge distribution varied even more markedly compared to CN-KI and CN-KI_3, indicating enhanced photo-generated carrier separation. These findings substantiate that multiple iodine species-constrained insertion significantly improves CN's photoactivity, facilitating more effective oxidant activation.

Work functions for the various model systems were assessed to deepen our understanding of electron dynamics. The measured work functions for CN, CN-KI, CN-KI_3, and CN-KI-I_3 were 5.59, 4.31, 4.84, and 4.39 eV, respectively (Fig. 1d–g). These measurements reveal that the insertion of different iodine species between CN layers promotes charge transfer and electron excitation, resulting in increased carrier concentrations. Notably, clever modulation was achieved through the simultaneous introduction of I^- and I_3^-. This process must be meticulously managed to prevent weak catalyst binding to free electrons, potentially leading to surface recombination of carriers if not promptly utilized. Density of States (DOS) calculations were conducted to analyze the variations in electronic band structures and band gaps across these model systems (Fig. 1h–k). The conduction band (CB) of bulk CN was formed by the hybridization of C and N atom 2*p* orbitals, while the valence band (VB) consisted primarily of N 2*p* orbitals. The introduction of iodine species significantly altered the band structure of modified CN.

For instance, introducing I^- or I_3^- in CN-KI and CN-KI_3 resulted in a downward shift of the CB and induced midgap energy levels within the band gap. CN-KI-I_3, which incorporates both I^- and I_3^-, maintained a suitable downward shift of the CB while generating additional midgap energy levels. These new midgap states facilitated the transition of photo-generated electrons from the VB to the CB by lowering transition barriers, thereby enhancing the efficient participation of photo-generated carriers in the catalytic reaction. The formation energy of these model systems was further explored to verify their structural stability and the feasibility of in-situ reconstruction (Fig. 1l). The formation energies for CN, CN-KI, CN-KI_3, and CN-KI-I_3 were −3.81, −2.95, −3.16, and −5.52 eV, respectively. Higher formation energies for CN-KI and CN-KI_3 indicated less structural stability, presenting excellent opportunities for in-situ reconstruction. As expected, CN-KI-I_3 exhibited the lowest formation energy among the models, suggesting that the preparation of a "pre-catalyst" by inserting I^- and K^+ into CN interlayers, followed by the in-situ introduction of I_3^- through subsequent photo-Fenton-like reactions for catalyst reconstruction, is thermodynamically favorable. Differential charge density calculations illustrated electron transfer pathways for CN-KI, CN-KI_3, and CN-KI-I_3 (Fig. 1m–o and Supplementary Fig. 2), with electron accumulation and consumption depicted in red-brown and green colors, respectively. CN-KI-I_3 demonstrated more robust and diverse electron movement compared to CN-KI and CN-KI_3, indicating enhanced intrinsic photoactivity. This enhancement could provide more electrons for oxidant activation, facilitating the generation of active species necessary for the efficient purification of contaminated water bodies.

In summary, these computational insights affirm the strategic design of "pre-catalysts" by constraining K^+ and I^- between CN layers, demonstrating their robust intrinsic photocatalytic activity and the feasibility of in-situ introduction of I_3^- for effective catalyst reconstruction.

Comprehensive assessment of the activity and stability of predetermined systems

To validate the exceptional catalytic activity and superior photostability of the predetermined reaction system, synthesized samples were tested for their ability to remove the antibiotic sulfamethoxazole (SMX) by activating periodate (PI) (Supplementary Fig. 3). Notable variations in SMX removal efficiency under different experimental conditions were observed (Fig. 2a and Supplementary Table 2). SMX adsorption on CN-KI was minimal (Supplementary Fig. 4), and PI alone exhibited no oxidation capability, underscoring the challenge of spontaneously generating active species. In the PI/Vis and CN-KI/PI systems, SMX removal efficiencies were 11.02% and 12.05%, respectively, indicating that neither visible light alone nor CN-KI effectively activated PI (Supplementary Fig. 5a). Furthermore, the CN/PI/Vis system achieved a modest 15.42% efficiency for SMX, underscoring the low activity of bulk CN. However, the CN-KI/Vis system demonstrated a removal efficiency of 32.18%, attributed to the enhanced photocatalytic performance of the catalyst, albeit still limited. Remarkably, the CN-KI/PI/Vis system achieved an impressive 99.14% removal efficiency for SMX, demonstrating the substantial formation of reactive oxygen species (ROS). Additionally, the SMX removal correlated positively with PI consumption, confirming a close relationship between catalytic oxidation and PI activation (Supplementary Fig. 5b). The quantitative kinetic assessment revealed that the degradation pseudo-first-order rate constant (*K*) for SMX in the CN-KI/PI/Vis system was 0.5681 min^{-1}, 12.32 to 6.48 times higher than that in other comparative systems. Moreover, the mineralization capacity in the CN-KI/PI/Vis system was found to be 7.65–61.99 times greater than in other systems (Supplementary Fig. 6). SMX removal in the CN-KI/PI/Vis system also exceeded that in individual iodine-doped and potassium-doped samples by 5.21 and 56.81 times, respectively, highlighting the synergistic effect of iodine and potassium in enhancing the activity of bulk CN (Supplementary Fig. 7). These results indicate that dual-site constrained interlayer insertion of K^+ and I^- could significantly enhance CN's ability to activate PI under visible light irradiation.

Further analysis of the effect of KI co-polymerization amount on the photocatalytic activation of PI showed that within a specific range, SMX removal was positively correlated with the amount of KI co-polymerization (Supplementary Fig. 8). The optimal *K* value for SMX removal was identified at CN-KI-4. However, higher levels of KI co-polymerization reduced efficiency, likely due to excessive KI disrupting CN's intrinsic structure. Subsequent tests to assess the effects of catalyst and PI doses on SMX removal exhibited a similar trend (Supplementary Figs. 9, 10). Considering kinetic constants and cost-efficiency, the optimal conditions for future experiments were determined to be a catalyst concentration of 0.2 g L^{-1} and an oxidant concentration of 1 mM.

In the context of optimized process parameters, the practical application potential of the CN-KI/PI/Vis system was extensively evaluated. This system demonstrated remarkable adaptability across a broad pH range of 5.0–11.0 (Supplementary Fig. 11), maintaining high and consistent removal efficiency across various water matrices, with different concentrations of co-existing anions and in diverse organic matter environments (Fig. 2b and Supplementary Figs. 12–20 and Supplementary Tables 7–10). Notably, it achieved rapid decolorization of Rhodamine B (RhB) under natural sunlight (Supplementary Fig. 21), and effectively activated various categories of structurally asymmetric oxidants to remove multiple types of organic pollutants (Fig. 2c and Supplementary Fig. 22). Additionally, the degradation kinetic constant of the CN-KI/PI/Vis system surpassed those reported for similar systems in the literature (Fig. 2h illustration and Supplementary Table 13), showcasing its robust activity and adaptability for wastewater remediation.

Subsequent evaluations focused on the recycling performance of the CN-KI/PI/Vis system under various conditions to assess the balance

https://doi.org/10.1038/s41467-025-58392-3

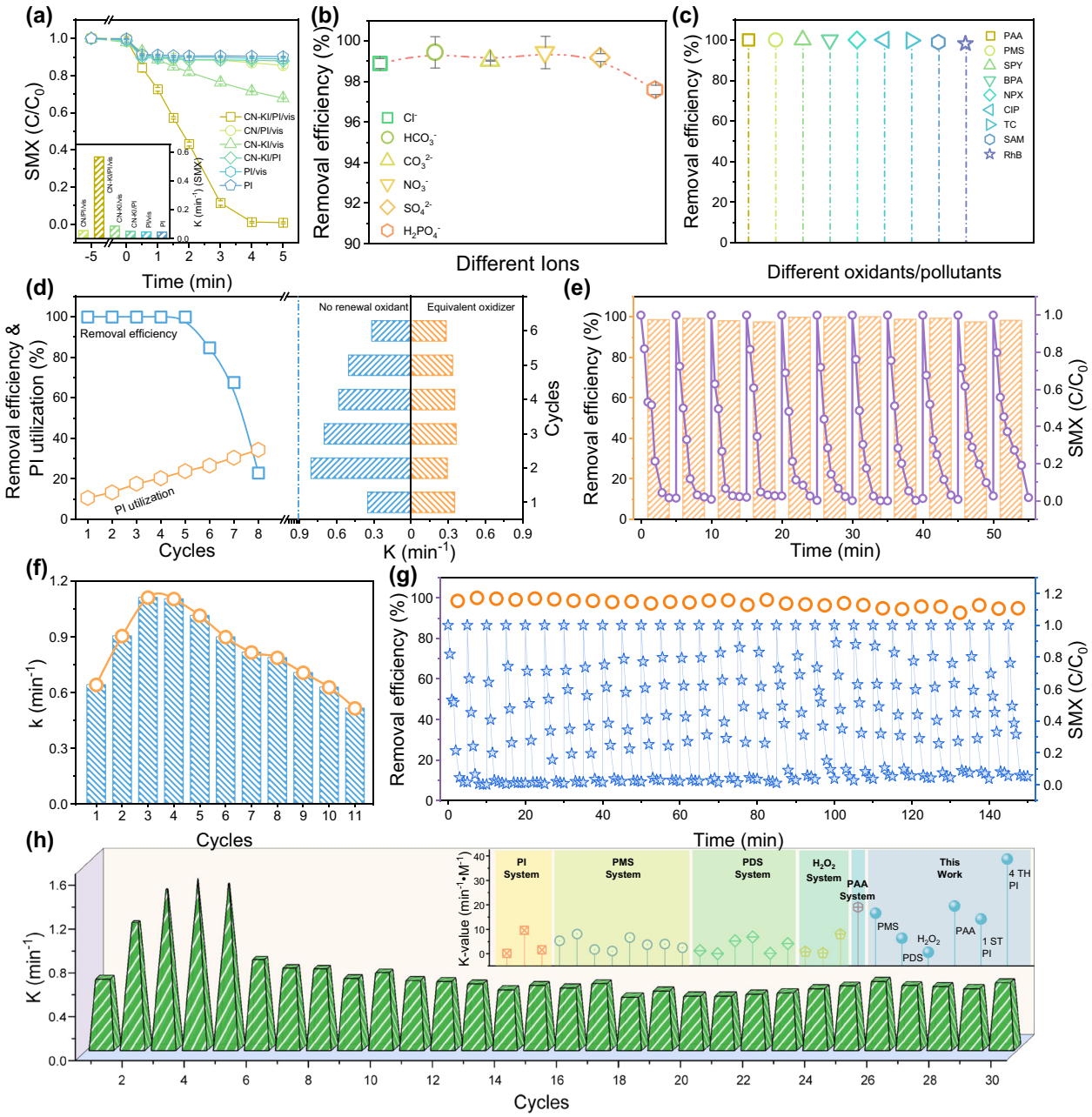

Fig. 2 | Catalytic activity and stability of the reconstructed system. **a** Degradation efficiency and kinetic rate constants for SMX in various systems. **b**, **c** Effect of different ions and oxidants on SMX removal in the CN-KI/PI/Vis system and efficiency across various pollutants. The bar chart represents the removal efficiency of SMX in the presence of various coexisting substances. All error bars in the figure represent the standard deviation from three replicate experiments. **d**, **e** Cyclical degradation of SMX in the CN-KI/PI/Vis system without oxidant replenishment. **f**, **g** Cyclical degradation of SMX in the CN-KI/PI/Vis system without catalyst replenishment. **h** Cyclical degradation of SMX in the CN-KI/PI/Vis system with replenishment of both oxidant and catalyst.

between catalytic activity and stability during the photoactivation of PI. Successive SMX degradation experiments, conducted without replenishing the oxidant, demonstrated that the CN-KI samples sustained five cycles of stable and efficient recycling (Fig. 2d). A notable decrease in efficiency during the sixth cycle was attributed to diminished oxidant concentration within the system. Intriguingly, the degradation rate constant (K) for SMX exhibited an increasing and then decreasing trend across these cycles, consistently surpassing that of the control system with the same oxidant amount (Fig. 2e, Supplementary Figs. 23, 24 and Table 14), highlighting a dynamic enhancement in the catalytic activity that effectively compensated for activity loss due to oxidant depletion. Additional recycling experiments, conducted without refreshing the catalyst, mirrored this pattern (Fig. 2f). Over 11 cycles, the system maintained an SMX removal efficiency exceeding 97.39%. The K value displayed an initial increase, followed by a decrease, with the ninth cycle still exhibiting higher activity than the first (Fig. 2g and Supplementary Table 15). These results confirmed the dynamic activity enhancement in the CN-KI samples, where the increased activity sufficiently offsets the loss caused by reduced catalyst content.

Encouraged by these promising results, the photo-stability of the CN-KI/PI/Vis system was further assessed under conditions of simultaneous catalyst and oxidant renewal. Throughout 30 consecutive cycles, the system consistently achieved SMX removal efficiencies exceeding 94.66% (Fig. 2h and Supplementary Table 16). The K for SMX removal demonstrated an initial increase, followed by a decrease and

https://doi.org/10.1038/s41467-025-58392-3

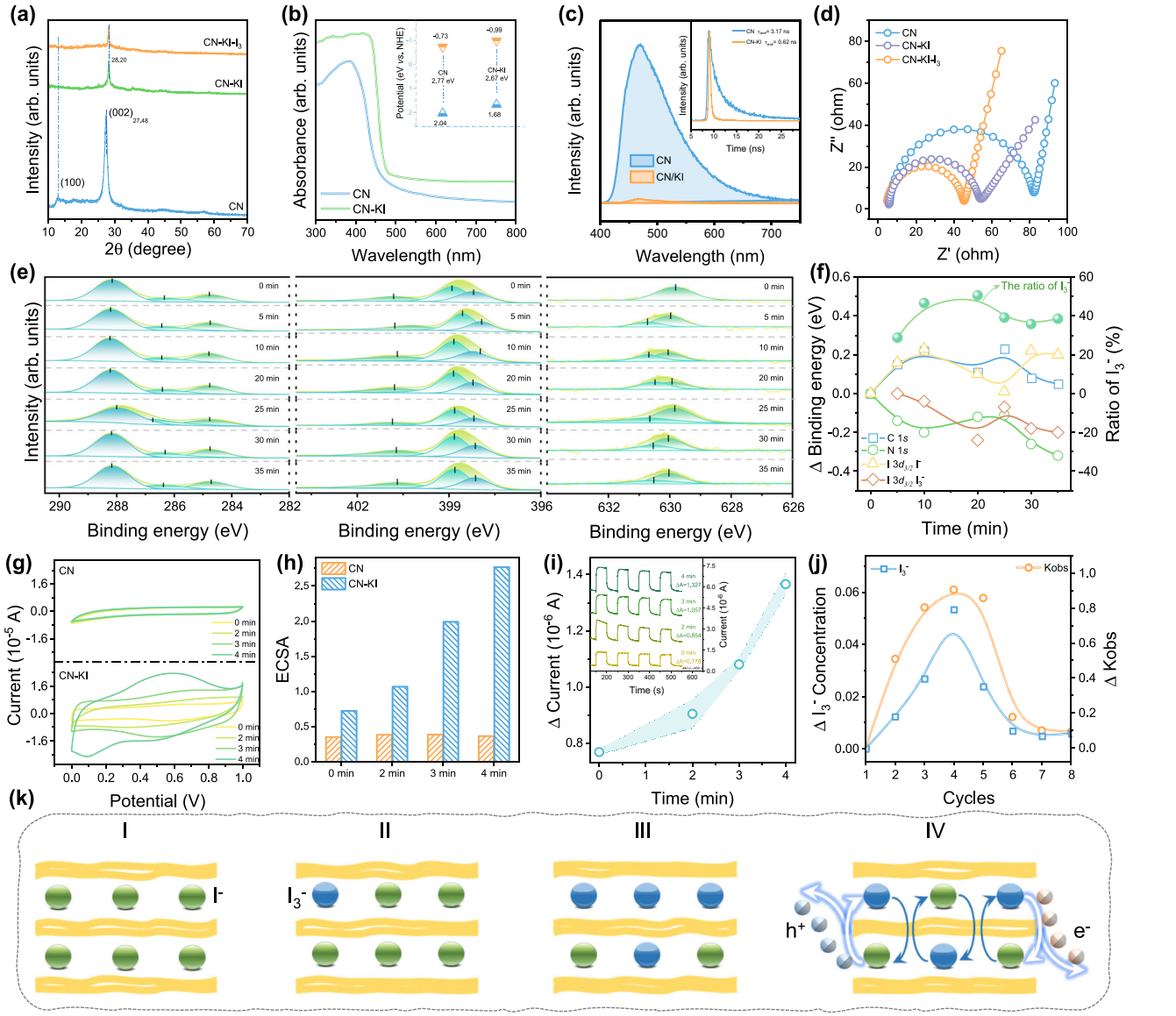

Fig. 3 | Sample characterization and dynamic reconstruction insights. a XRD patterns of CN, CN-KI, and CN-KI-I_3. **b**, **c** UV-vis DRS and PL spectra of CN and CN-KI. **d** Electrochemical impedance spectra of CN, CN-KI, and CN-KI-I_3. **e**, **f** *Semi*-in-situ XPS spectra of CN-KI. **g**, **h** *Semi*-in situ CV curves and electrochemically active surface area (ECSA) measurements for CN and CN-KI. *Semi*-in-situ photocurrent curves (**i**) and *semi*-in-situ UV-vis absorption spectra (**j**) of CN-KI. The error bands in the figure represent the standard deviation between three different time points. **k** Schematic illustration of dynamic reconstruction processes in the pre-catalyst CN-KI during the photoreaction.

eventual stabilization, yet it remained above initial levels throughout the test period (Fig. 2h). This exemplary cycling performance redefines the concept of 'stability' within the realm of photo-Fenton-like wastewater purification, highlighting the CN-KI/PI/Vis system's exceptional efficacy and resilience.

Identification of catalysts for precise synthesis and in-situ reconstruction properties

To ascertain whether the simultaneous enhancement of photoactivity and stability was associated with dynamic catalyst reconstruction, a comprehensive series of characterizations was performed on various samples. Scanning electron microscopy (SEM) was utilized to evaluate morphological differences among CN, CN-KI, and CN-KI-I_3 (used CN-KI) (Supplementary Fig. 25). The morphologies of CN and the various CN-KI samples were similar, and no significant morphological differences were observed in CN-KI-I_3, suggesting that morphological changes did not contribute to enhanced activity. X-ray diffraction (XRD) analysis further investigated the crystal structures of these samples (Fig. 3a and Supplementary Fig. 27). The CN diffraction peaks at 12.92° (100) and 27.48° (002) represent the in-plane and interlayer stacking of heptazine units, respectively[40]. Upon the introduction of K^+ and I^-, the (100) plane's diffraction peak disappeared, and the (002) plane's peak shifted and weakened. These noticeable changes suggest that K^+ and I^- were intercalated into the in-plane and interlayers of CN, disrupting the ordered structure of in-plane heptazine units and altering the interlayer interactions. Excessive K^+ and I^- introduction severely weakened the (002) plane diffraction peak, indicating a significant structural degradation of CN and a corresponding decrease in photocatalytic activity.

Fourier Transform Infrared (FT-IR) spectra across various samples showed similar vibrational peaks, with characteristic vibrations at 820, 1100–1700, and 3000–3500 cm^{-1}, attributed to triazine ring units, C=N heterocycles, and N-H groups, respectively[41] (Supplementary Fig. 28). A distinct peak at ~2178 cm^{-1} in modified CN, indicative of the cyano

group (-C≡N), likely resulted from co-polymerization with KI. Although FT-IR spectra revealed no significant differences between CN-KI and CN-KI-I_3, XRD analysis showed weaker diffraction peaks associated with the (002) crystal plane in CN-KI-I_3, suggesting altered interlayer interactions. Moreover, a smaller BET surface area and pore size in CN-KI compared to CN ruled out an increase in active sites (Supplementary Fig. 29 and Supplementary Table 17). Further Ab Initio Molecular Dynamics (AIMD) simulations confirmed the thermal stability of CN-KI and CN-KI-I_3. Both materials maintained their crystal structure integrity throughout simulations lasting up to 20 ps, effectively ruling out any alterations in activity caused by structural depolymerization of the catalyst (Supplementary Fig. 30). Therefore, the remarkable simultaneous enhancement of activity and stability in CN-KI-I_3 could be attributed to the catalyst's internal dynamic reconstruction.

X-ray photoelectron spectroscopy (XPS) was used to further analyze the chemical composition and bonding structure of the samples. The XPS spectrum of modified CN, unlike that of pure CN, displayed the presence of K and I elements, along with C and N, indicating successful integration into the CN structure through co-polymerization with KI (Supplementary Figs. 31–35 and Supplementary Table 18–21). SEM-energy dispersive X-ray spectroscopy (SEM-EDS) confirmed a uniform distribution of C, N, K, and I across the samples (Supplementary Fig. 36). Additionally, high-resolution X-ray photoelectron spectroscopy (XPS) spectra of C 1*s* and N 1*s* provided detailed insights into the chemical environment within the samples (Supplementary Figs. 31–35). Distinct convolution peaks were observed for C 1*s* at ~288, 286, and 284 eV, corresponding to the N-C=N, C-NH_x/C≡N, and C-C bonds, respectively[42]. For N 1*s*, prominent peaks at about 400, 399, and 398 eV were associated with C-N-H, N-C_3, and C-N=C bonds, respectively[15]. These slight fluctuations in binding energy among different catalysts underscore the effective optimization of the catalyst's electron density through modification, while preserving the fundamental structure of CN intact—a crucial factor in maintaining its performance. Notably, the modified CN exhibited an increased percentage of C-NH_x/C≡N compared to bulk CN, a change attributed to enhanced deprotonation kinetics of terminal amino groups. These observations highlight the impact of KI modification on CN, corroborating findings from FT-IR analyses. Additionally, shifts in the binding energies of K 2*p* and I 3*d* spectra across the various modified CN samples suggest that the K and I elements were homogeneously integrated into the CN structure, rather than existing as separate KI compounds. This integration was crucial in enhancing the photocatalytic activity and stability of the modified CN, demonstrating the transformative effect of dual-site insertion on the material's properties.

Assessing the optical properties and carrier transfer kinetics of pre-catalysts

Optical properties are fundamentally connected to the catalytic activity of photocatalysts. The influence of KI co-polymerization on the electronic and optical properties of photocatalysts was elucidated using UV-visible diffuse reflectance spectroscopy (UV-vis DRS) (Fig. 3b). Compared to bulk CN, CN-KI exhibited significantly enhanced light absorption due to n-π* and π-π* electronic transitions. This enhancement suggests that the introduction of K^+ and I^- effectively improves the catalyst's light capture capabilities[43]. Analysis of Tauc plots and Mott-Schottky (MS) plots revealed significant alterations in the bandgap structure and band edge positions of CN-KI (Supplementary Figs. 37, 38). Specifically, CN-KI exhibited a narrower bandgap (2.67 eV compared to CN's 2.77 eV) and a lower CB position (−0.99 eV for CN-KI versus −0.73 eV for CN). These modifications demonstrate that KI co-polymerization not only enhances the photocatalyst's light capture ability but also boosts its electron-donating capacity, thereby increasing the driving force for oxidant activation.

To further investigate the efficiency of photo-generated carrier separation, the impact of KI co-polymerization on PI activation by modified CN was assessed. Notably, CN-KI showed virtually negligible photoluminescence (PL) emission peaks compared to CN, clearly indicating a significant reduction in the recombination rate of photo-generated carriers (Fig. 3c). Time-resolved photoluminescence (TR-PL) measurements revealed that the average lifetimes of carriers were significantly reduced in CN-KI (0.62 ns) compared to CN (3.17 ns). This reduction in lifetime indicates rapid exciton dissociation, enhanced by the interlayer insertion of K^+ and I^-. Such enhancement could improve the migration and diffusion of photo-generated carriers, thereby boosting catalytic activity. Additionally, electrochemical measurements indicated a higher photocurrent response and a smaller arc radius in CN-KI compared to CN (Fig. 3d and Supplementary Fig. 39), confirming more efficient carrier transfer. The enhanced mobility of photo-generated carriers suggests that more electrons participated in generating active species, which facilitated the rapid purification of polluted wastewater.

Deciphering the dynamic I^-/I_3^- redox mediator reconstruction process

To elucidate the mechanism behind the dynamic activity enhancement of CN-KI, a series of *semi*-in-situ characterization analyses were conducted. Utilizing *semi*-in-situ XPS technology, we observed the formation and operation of I^-/I_3^- redox mediators within the catalyst, providing crucial evidence for its dynamic reconstruction (Fig. 3e–h, Supplementary Fig. 40 and Tables 22–24). Specifically, we analyzed changes in binding energy, where an increase indicates electron loss, and a decrease suggests electron gain[44]. Initially, the electron dynamics within the system were primarily driven by carbon and nitrogen, as evidenced by symmetric changes in their binding energies, reflecting a balanced electron gain and loss. Upon initiation of the catalytic reaction, I^- was oxidized by photo-generated holes to form I_3^-. This oxidation process initially intensified, as indicated by an increasing percentage of I_3^-, but eventually decreased and stabilized as the reaction progressed.

The observed fluctuations in the system, alongside the minimal leaching of iodine and the maintenance of a relatively stable total iodine content throughout the catalytic cycle, suggest that the I_3^-, produced by the oxidation of I^-, were reduced back to I^- instead of being expelled from the catalyst (Supplementary Fig. 41). The consistent increase in binding energy for I^- and the corresponding decrease for I_3^- provided direct evidence of their mutual conversion. Furthermore, the reduction rate was influenced by the concentration of I_3^-, highlighting a dynamic interplay between the formation and conversion of I_3^-. This interconversion resulted in significant changes in electron flow within the system during the mid-reaction stages, characterized by a sharp decrease in electron output from carbon and electron intake by nitrogen. In the later stages of the reaction, electron flow stabilized and was predominantly maintained by the interconversion of I^- and I_3^-, as their binding energy changes remained relatively constant. Unlike the initial fluctuations observed for carbon and nitrogen, the binding energy changes for I^- and I_3^- exhibited a sustained symmetrical distribution, indicating a stable conversion between these species as the reaction progressed.

These findings validate the cyclical process where I^- generating I_3^-, stabilizing into a dynamic I^-/I_3^- redox mediator in the later stages of the reaction, culminating in the catalyst's dynamic reconstruction. This reconstruction improved the migration efficiency and utilization of photo-generated carriers within the catalyst. The marked increase followed by a decrease in electrons gained by I_3^- clearly demonstrates the ability of the I^-/I_3^- redox mediators to temporarily store electrons not immediately involved in the reaction and release them in subsequent cycles. This mechanism significantly enhances the photocatalytic activity and stability of the system.

The *semi*-in-situ cyclic voltammetry (CV) analysis provided compelling evidence for the dynamic reconstruction of the catalyst (Fig. 3i). The CV curves for CN remained consistent across various time scales, indicating minimal changes in the electrochemical active surface area (ECSA) (Fig. 3j). In stark contrast, CN-KI exhibited clear oxidation peaks indicative of the oxidation of I^- to I_3^-, and reduction peaks corresponding to the conversion of I_3^- back to I^-, all within the same time frame. As the photoactivation of PI progressed, these peaks became more pronounced and underwent significant changes, accompanied by a gradual expansion of the ECSA. Additionally, a stepwise enhancement of the photocurrent response was observed in the *semi*-in-situ i-t curves (Fig. 3k), vividly demonstrating the dynamic reconstruction of the "pre-catalyst" during the reaction through the spontaneous formation of I^-/I_3^- redox mediators. This dynamic reconstruction of the catalyst led to a secondary photoactivity enhancement, evidenced by a more robust photocurrent response and reduced impedance in CN-KI-I_3 compared to CN-KI.

To further clarify the relationship between the in-situ formation of I^-/I_3^- redox mediators and the catalyst's activity and stability, we monitored the dynamic changes in I_3^- concentration across different cycles using *semi*-in-situ UV-Vis absorption spectroscopy (Fig. 3i and Supplementary Fig. 42). Initially, the I_3^- concentration increased and subsequently decreased, reaching equilibrium after 8 cycles. This confirmed the dynamic transformation of I^-/I_3^- redox mediators, aligning with the *semi*-in-situ XPS findings. Furthermore, the dynamic trend of I_3^- concentration closely mirrored the changes in the *K* value of SMX degradation during the cycling treatment, confirming a positive correlation between these variables.

Overall, these results substantiate that the dynamically enhanced activity and exceptional photo-stability of the CN-KI/PI/Vis system stem from the in-situ reconstruction of the photocatalyst by the spontaneously formed I^-/I_3^- redox mediators within CN-KI. This discovery provides valuable insights and opens more opportunities for designing efficient and durable CN-based photocatalysts.

Determination and quantification of active species in reconstructed systems

The satisfactory catalytic efficiency led us to identify the dominant active species within the system. We used EDTA-2Na, *L*-histidine, p-BQ, and TBA as scavengers, specifically targeting photo-generated holes (h^+), singlet oxygen ($^1O_2$), superoxide anions radicals ($^{\bullet}O_2^-$), and hydroxyl radicals ($^{\bullet}OH$), respectively[45] (Supplementary Fig. 43). When EDTA-2Na, *L*-histidine, and p-BQ were individually introduced to the CN-KI/PI/Vis system, SMX removal was significantly reduced by 60.82%, 86.47%, and 91.58%, respectively, highlighting the critical roles of h^+, $^1O_2$, and $^{\bullet}O_2^-$. Conversely, the addition of TBA had no significant effect, suggesting a minor role for $^{\bullet}OH$. This pattern was replicated in the CN-KI/Vis system using different quenchers, reinforcing these findings (Supplementary Fig. 44).

Electron spin resonance (ESR) measurements further corroborated these findings. The TEMPO-h^+ signal intensity decreased after illumination and increased upon adding SMX, demonstrating h^+ generation in the CN-KI/PI/Vis system post-irradiation and its subsequent utilization in oxidizing SMX. Similar trends were observed with TEMP-$^1O_2$ and DMPO-$^{\bullet}O_2^-$ (Fig. 4a–c). The distinct signal peaks observed under both dark and illuminated conditions significantly enhanced the catalyst's activation for PI. The addition of SMX notably reduced the signal intensities of $^1O_2$ and $^{\bullet}O_2^-$, confirming their role in SMX oxidation. Further investigation explored the potential formation of iodine-active species, such as $IO_3^{\bullet}$, HOI, I_2, I_3^-, and iodine disinfection by-products (I-DBPs) during PI activation (Supplementary Figs. 45–48). Among these, only $IO_3^{\bullet}$ was detected, and its concentration remained consistently low, confirming its limited role in the removal of SMX. Importantly, this minimized the possibility of I-DBPs formation, as iodine-active species like HOI, I_2, I_3^- were more reactive in oxidizing natural organic matter to form I-DBPs[46–49]. To substantiate the limited formation of I-DBPs further, we analyzed the degradation products of the CN-KI/PI system both with and without the presence of humic acid. The results indicated that the degradation products were nearly identical under both conditions, effectively ruling out the likelihood of I-DBPs formation during SMX degradation in the CN-KI/PI/Vis system.

To comprehensively assess the impact of dynamic catalyst reconstruction, we quantified PI consumption and the concentration of ROS generated during the process (Fig. 4d–f and Supplementary Figs. 49–52). Although the types of dominant active species remained consistent, PI consumption initially increased and then decreased as reconstruction progressed. Correspondingly, the concentration of the dominant active species, $^{\bullet}O_2^-$, initially increased and then stabilized. These trends were attributed to the in-situ introduction of I^-/I_3^- redox mediators in the reconstructed system, which enhanced the photocatalyst's intrinsic activity. In contrast, the concentration of $^1O_2$ initially increased, then decreased, and finally stabilized, a key factor in the observed reduction of the SMX degradation rate after the fourth cycle. Overall, these trends correlate well with the fluctuations in I_3^- concentration during various cycles (at different reconstruction times) and the changes in the *K* value for SMX degradation across cycles. These results illustrate the in-situ dynamic reconstruction of CN-KI during reactions, which directly enhances its activity. This enhancement enables the newly formed catalytic system to generate more ROS than the pre-catalytic system, ensuring both high activity and exceptional stability.

Using theoretical calculations, we further explored the mechanisms behind the enhanced catalytic activity and photo-stability of the CN-KI(I_3)/PI/Vis system. Key factors such as the adsorption energy (E_{ads}) of PI molecules on the catalyst and the I-O bond length are critical for PI activation. E_{ads} indicate the thermodynamic feasibility of PI binding to the catalyst, reflecting the strength of their interaction, while the I-O bond length suggests the ease with which PI can decompose. The adsorption energies (E_{ads}) for CN, CN-KI, CN-KI_3, and CN-KI-I_3 with PI were measured at −1.41, 1.94, −2.08, and −2.19 eV, respectively (Fig. 4k). Notably, PI exhibited a suitable E_{ads} on CN-KI-I_3, suggesting that the moderate binding affinity between PI and the catalyst played a crucial role in enhancing catalytic activity and stability. Differential charge density maps visually illustrated these interactions, revealing more localized electron clouds and diverse electron movement pathways in CN-KI-I_3/PI (Fig. 4g–j and Supplementary Fig. 53). These observations suggest that the CN-KI-I_3/PI model exhibited higher electron mobility and faster reaction rates post-binding. However, the shortest I-O bond length in the CN-KI-I_3/PI model indicated a less favorable pathway for PI decomposition (Supplementary Fig. 54). Additionally, further energy barrier calculations for the production of $^1O_2$ from PI decomposition challenged initial assumptions. In the rate-determining step ($^*IO_4^- \rightarrow {}^*IO_3^- + {}^*O$), the energy required for CN-KI-I_3 was unexpectedly higher compared to CN, CN-KI, and CN-KI_3. This finding contrasted with the high reaction rate constants observed in the CN-KI-I_3/PI/Vis system (Fig. 4k and Supplementary Fig. 55). Interestingly, the utilization efficiency of PI remained low across all designs. Additionally, the production trends of $^{\bullet}O_2^-$ and $^1O_2$ in the CN-KI(I_3)/PI/Vis system were closely aligned. Crucially, quantitative analysis of IO_3^- ($IO_3^{\bullet}$) revealed that the consumed PI was almost entirely converted to $IO_3^{\bullet}$, with no contribution to $^{\bullet}O_2^-$ and $^1O_2$ production (Supplementary Fig. 45). This suggested an alternative catalytic mechanism where the primary sources of the dominant active species, $^{\bullet}O_2^-$ and $^1O_2$, originated from the reduction processes of dissolved oxygen rather than PI decomposition. The contrasting behavior in SMX degradation under N_2 and O_2 atmospheres observed in the CN-KI/PI/Vis system further supported this catalytic mechanism (Supplementary Fig. 56).

Given these surprising findings, we proposed a revised catalytic mechanism for the reconstructed systems (Eqs. 1–5 and

Supplementary Fig. 58). In this updated model, PI functioned not as a traditional oxidant but as an electron acceptor. This role was substantiated by the increased electrical current observed upon its complexation with CN-KI-I_3 (Supplementary Fig. 59). The van der Waals interaction between PI and CN-KI-I_3 formed a complex that significantly enhanced the intrinsic catalytic activity, facilitating the oxygen reduction reaction to generate more $^{\bullet}O_2^-$ and $^1O_2$. Together with the accumulated photo-generated holes, these reactive species effectively purify contaminated water, providing a robust and efficient mechanism for wastewater treatment.

$$^{*}CN - KI - I_3 + PI \rightarrow {}^{*}CN - KI - I_3/PI \quad (1)$$

$$^{*}CN - KI - I_3/PI + h\nu \rightarrow h^+ + e^- \quad (2)$$

$$O_2 + e^- \rightarrow {}^{\bullet}O_2^- \quad (3)$$

$$^{\bullet}O_2^- + h+ \rightarrow {}^1O_2 \quad (4)$$

$$\text{Pollutants} + h^+ / {}^{\bullet}O_2^- / {}^1O_2 \rightarrow CO_2 + H_2O \quad (5)$$

Environmental adaptability assessment and outdoor scale-up applications

After elucidating the mechanisms behind the remarkable photoactivity and stability of the CN-KI/PI/Vis system, we evaluated the toxicity of SMX degradation products. Degradation pathways were inferred from liquid chromatography-mass spectrometry (LC-MS) analyses (Supplementary Figs. 60, 61 and Supplementary Table 29). Furthermore, the ecotoxicity of all degradation intermediates was predicted using the ECOSAR model and the Toxicity Estimation Software Tool (T.E.S.T)[50] (Fig. 5e and Supplementary Fig. 62 and Supplementary Table 30). The findings demonstrated that the acute (LC_{50}), chronic (CHV) toxicity, mutagenicity, bioaccumulative toxicity, and developmental toxicity of most intermediates were lower than those of the parent pollutant, indicating that the SMX removal process in the CN-KI/PI/Vis system effectively reduced toxicity. Additionally, real toxicity evaluations of the degradation products were conducted through biological assays, including cultures of *Escherichia coli*, Zebrafish embryo cultivation, and wheat seed germination tests (Fig. 5a–d and Supplementary Figs. 63–65). Zebrafish embryo hatching experiments, utilizing water treated by various systems as the exposure solution, revealed lethal symptoms in embryos exposed to the original SMX and those treated with the CN/PI/Vis and CN-KI/Vis systems. This indicates substantial animal toxicity in the original SMX and inadequate detoxification by these systems. In contrast, Zebrafish embryos developed comparably to the control group in the CN-KI/PI/Vis system, affirming its efficacy from a zoological perspective. Similarly, in wheat seed germination tests using water treated by various systems, only seeds irrigated with water from the CN-KI/PI/Vis system exhibited root and shoot lengths comparable to the control, further validating its detoxification efficiency. Additionally, in *Escherichia coli* culturing experiments using detoxified water as the medium, the survival rates in water treated with the original SMX, CN/PI/Vis, CN-KI/Vis, and CN-KI/PI/Vis were 12.66%, 19.82%, 33.21%, and 89.27%, respectively. These comprehensive evaluations from predictive, animal, plant, and bacterial perspectives confirmed the effective detoxification of SMX by the CN-KI/PI/Vis system.

To address the challenge of recovering powdered catalysts from liquid phases, 10 mg of the CN-KI catalyst was immobilized on a sponge within a micro continuous-flow device that served as the reactor (25 cm^2). Wastewater was channeled through "U"-shaped tubing at a flow rate of 11.56 mL min^{-1} to assess photocatalytic oxidation (Supplementary Fig. 66). Benefiting from CN-KI's favorable in-situ dynamic reconstruction properties and the functionalization mechanism of PI, this setup consistently achieved 100% removal efficiency for RhB and at least 94% SMX removal during a continuous 24-h operation. This performance demonstrates CN-KI's exceptional long-term operational potential in immobilized systems (Fig. 5f, g).

To further evaluate the application potential of CN-KI in real-world settings, a larger continuous flow reaction device was constructed, measuring 900 cm^2 with a flow rate of 20.21 mL min^{-1}, and its oxidation performance was tested under natural sunlight (Supplementary Fig. 68). The optimized wastewater treatment system consistently achieved over 90% SMX removal across a sunlight irradiance range of 15.53–78.38 mW cm^{-2} (10 AM-8 PM). After sunset, despite the light intensity dropping to 2.23 mW cm^{-2}, the catalytic degradation of SMX continued, supported by the enhanced light absorption capacity of CN-KI and improvements in photocatalytic performance due to in-situ dynamic reconstruction. This capability was further validated by effective degradation under LED illumination at 4.41 mW cm^{-2} (Supplementary Fig. 69), demonstrating that LED-driven removal could effectively address the limitations of photocatalytic technology's nocturnal inoperability.

Evaluating the purification efficiency of real wastewater is essential for validating and optimizing proposed photocatalytic systems, offering significant reference value for industrial scale-up. To this end, simulated chemical wastewater was initially prepared using high-performance liquid chromatography effluent. The real-time removal efficiency of SMX was assessed using a plate-type continuous flow reactor with an effective area of 1 m^2, powered solely by sunlight (Fig. 6a–c and Supplementary Figs. 70, 71). Over a continuous 12-h operation, the system achieved satisfactory purification results at various flow rates, treating up to 28.8 L of wastewater and consistently maintaining SMX removal above 80% and TOC removal efficiencies above 48.67%.

Subsequently, a pilot-scale reactor was developed to further evaluate the industrial scalability of the CN-KI/PI/Vis system. This reactor, which included a 20 L tank and 300 mg of floating CN-KI catalysts, was tested using simulated chemical wastewater, medical wastewater from a hospital in Chongqing, China, and coking wastewater from Chongqing Iron and Steel Company (Fig. 6d–f and Supplementary Fig. 72). The floating design of the CN-KI catalysts significantly enhanced light penetration and mass transfer at the gas-liquid-solid three-phase interface, promoting rapid generation of active oxygen species via the oxygen reduction reaction. Within 30 min of reaction time, 97.01% of SMX was removed from the simulated chemical wastewater, with a TOC removal rate of 74.94% (Fig. 6g–i and Supplementary Table 31). Due to the enhanced mass transfer and the dynamic reconstruction of the CN-KI/PI system, the reactor demonstrated the ability to continuously treat at least 80 L of wastewater without needing to replace the catalyst or oxidant, maintaining a removal efficiency above 87.98%, thereby demonstrating significant potential for industrial application.

After 60 min of treatment with medical wastewater, the TOC removal rate reached 73.79%, and the chemical oxygen demand (COD) decreased from 100.95 mg L^{-1} to 20.95 mg L^{-1}, achieving a removal efficiency of 79.25% and meeting discharge standards. Ammonia nitrogen (NH_3-N) was reduced from 6.32 mg L^{-1} to 4.89 mg L^{-1}, with a removal efficiency of 22.57%, which further mitigated environmental risks (Fig. 6i and Supplementary Fig. 73). After 2 h of treatment in the pilot-scale reactor, the removal efficiencies for TOC, COD, and NH_3-N in coking wastewater were 57.25%, 61.56%, and 68.77%, respectively. TOC decreased from 355.6 mg L^{-1} to 152 mg L^{-1}, COD from 8650 mg L^{-1} to 3325 mg L^{-1}, and NH_3-N from 200.40 mg L^{-1} to 62.58 mg L^{-1}. Additionally, there were notable improvements in watercolor and salinity

https://doi.org/10.1038/s41467-025-58392-3

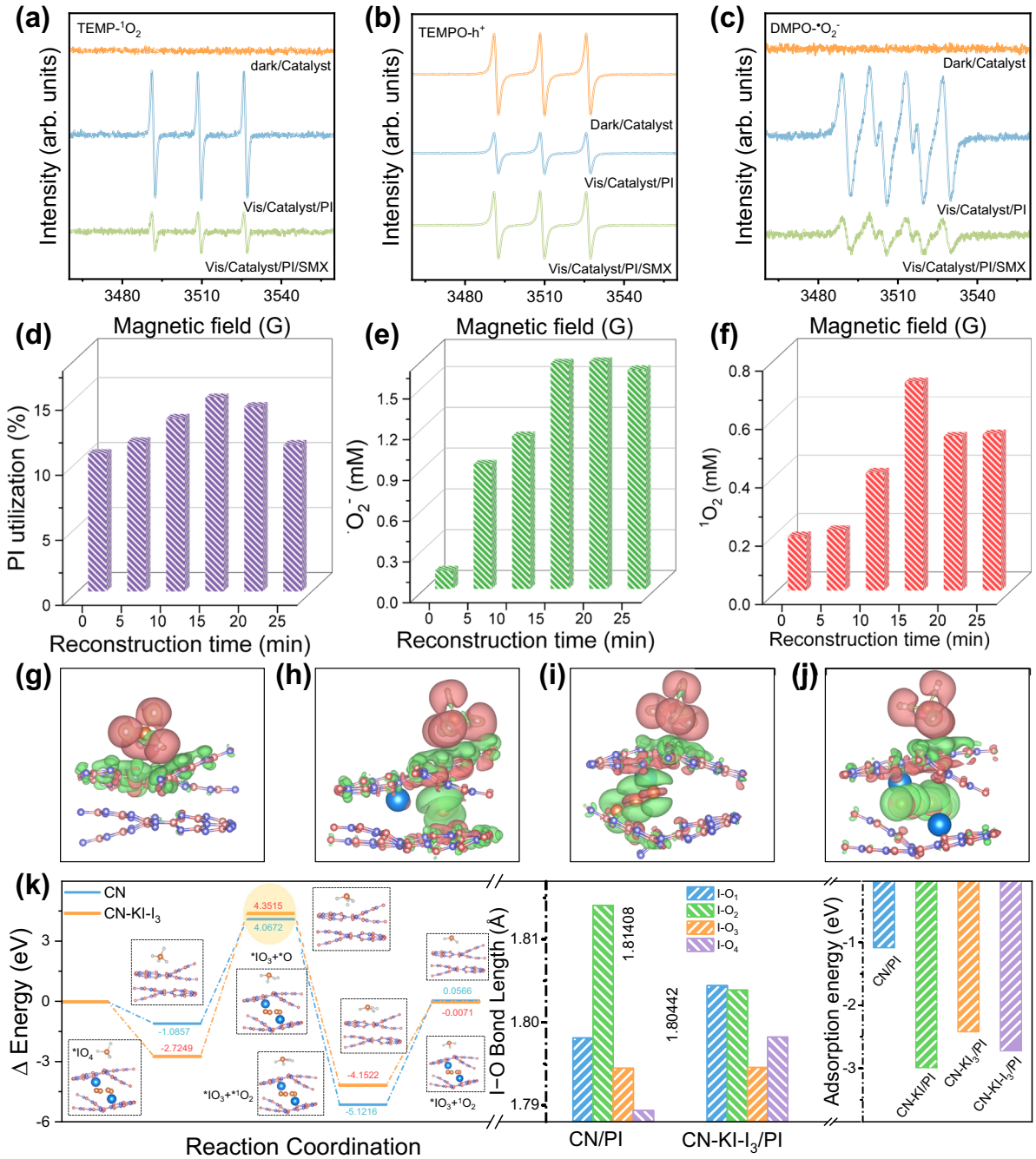

Fig. 4 | Active species identification and catalytic mechanism exploration. **a**–**c** EPR spectra depicting active species in the CN-KI/PI/Vis system. **d**–**f** Utilization rates of PI and ROS production at different stages of catalyst reconstruction. Electron density difference diagrams for CN/PI (**g**), CN-KI/PI (**h**), CN-KI$_3$/PI (**i**), and CN-KI-I$_3$/PI (**j**). **k** Energy diagrams for $^1O_2$ production from PI decomposition on CN and CN-KI-I$_3$; I-O bond lengths in CN/PI and CN-KI-I$_3$/PI; adsorption energies for various PI-catalyst complexes.

(Fig. 6i, Supplementary Fig. 74 and Table 31). These significant advancements relieved technical and economic pressures on subsequent treatment processes, confirming the industrial feasibility and scalability of the CN-KI/PI system.

In conclusion, the CN-KI/PI system, leveraging the advantages of in-situ dynamic restructuring and effectively overcoming light penetration limitations through its innovative floating design, demonstrated high activity and broad applicability across various scenarios. Furthermore, the dynamic reconstruction of CN-KI could be extended to H_2O_2 photocatalytic production, demonstrating its potential for multifunctional applications, particularly in the synthesis of high-value products (Supplementary Fig. 75).

Sustainability evaluation and cost analysis for industrial applications

To assess the primary costs and environmental impacts of the constructed catalytic system, an economic analysis was conducted based on the Electrical Energy per Order (EE/O) concept, accompanied by a preliminary Life Cycle Assessment (LCA). These assessments aimed to provide strategic optimization guidelines for potential industrial expansion. For comparative purposes, classical Fenton and O_3-based systems were utilized to purify simulated and real chemical wastewater. Notably, EE/O has been defined as the electrical energy required to reduce the concentration of low-level pollutants by one order of magnitude[51,52]. Although the total cost for

https://doi.org/10.1038/s41467-025-58392-3

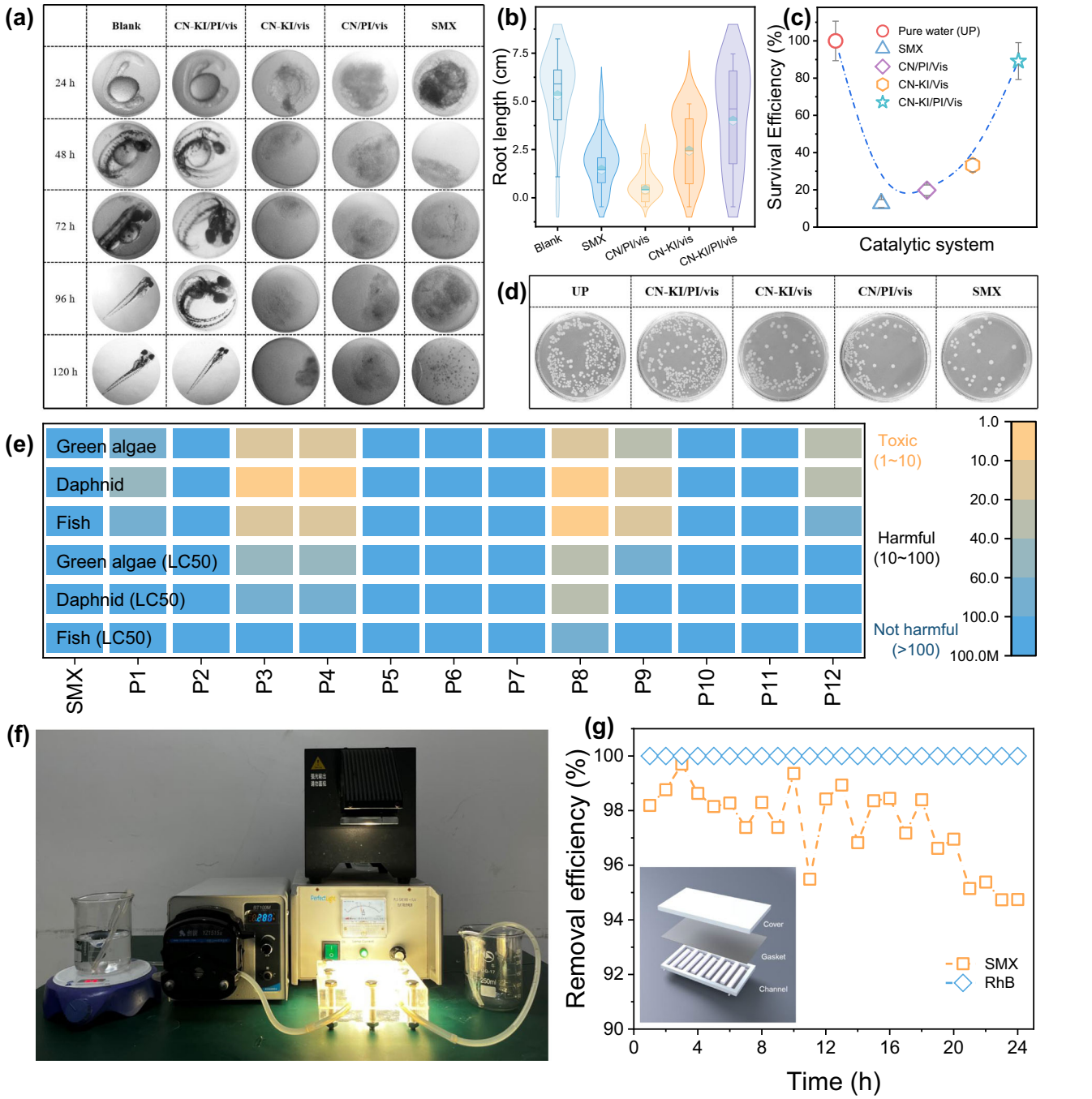

Fig. 5 | Environmental adaptability assessment. The survival rate of Zebrafish embryo development (**a**), growth of wheat (**b**) and the survival rate of *Escherichia coli* (**c**, **d**) in different systems. **e** Toxicity indicators of parent SMX and its degradation products. In the violin plot, the box represents the interquartile range (IQR) between the first and third quartiles, with the points inside the box indicating the mean value. The whiskers represent the minimum or maximum values within 1.5 times the IQR from the first or third quartile. Additionally, the error bars in (**c**) represent the standard deviation of three replicate experiments. **f**, **g** Indoor continuous flow photocatalytic reactors and its photocatalytic purification performance for RhB and SMX.

indoor purification using the CN-KI/PI system was higher, the operational cost for the CN-KI/PI/sunlight system in the outdoor pilot-scale reactor significantly decreased to 0.0297 kWh L^{-1}, which was lower than that of the widely recognized O_3 (0.085 kWh L^{-1}) and H_2O_2/O_3 systems (0.064 kWh L^{-1}) (Fig. 6j and Supplementary Table 32). It was important to note that while the Fenton system had a lower operational cost due to its reliance solely on reagents, its purification efficiency was less effective (Fig. 6h and Supplementary Figs. 77, 78). This lower efficiency was primarily due to the high content of alcohol species in the wastewater, which competed with the ·OH, diminishing their effectiveness. Moreover, this comparison highlighted that the CN-KI/PI system has a broader application range in water pollution control than the Fenton system. Focusing solely on the energy input from the light source, a comprehensive cost comparison was conducted between the CN-KI/PI/Vis system and reported photo-Fenton-like, iodine-based, and chlorine-based oxidation processes (Fig. 6j and Supplementary Fig. 79). The treatment cost for the CN-KI/PI/Vis system was notably low at only 0.405 kWh L^{-1}, significantly less than those reported for other photocatalytic systems. These comparative data underscored the CN-KI/PI/Vis system's practical feasibility, particularly for large-scale applications.

https://doi.org/10.1038/s41467-025-58392-3

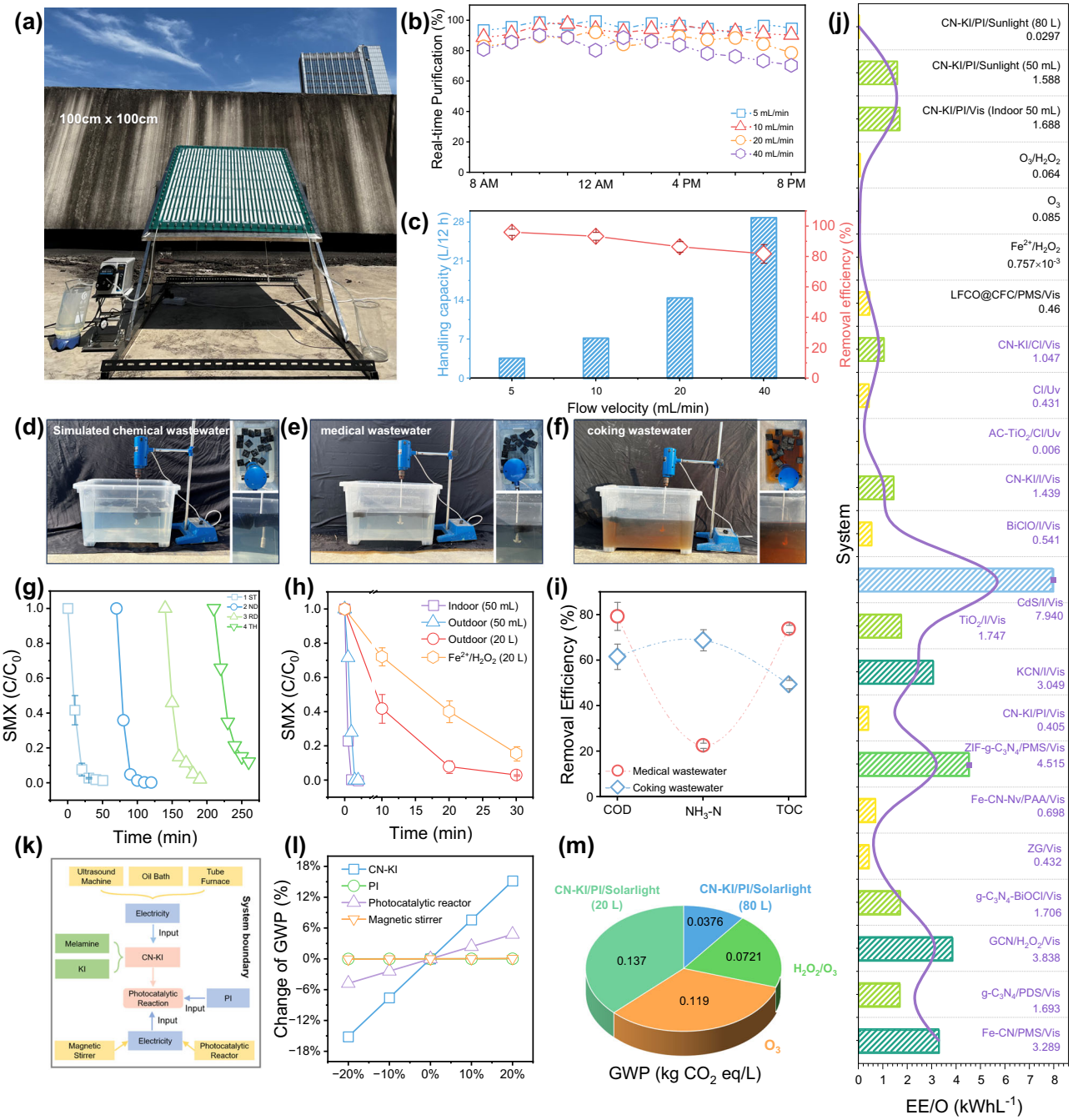

Fig. 6 | Evaluation of the potential for industrial-scale application. a Solar-powered square meter-scale plate continuous flow reactor. **b**, **c** The removal efficiency of simulated chemical wastewater in a square-meter-scale plate continuous flow reactor at different flow rates. **d**–**f** Pilot treatment devices for simulated chemical, real medical, and coking wastewater. **g** Cyclic purification performance of the solar-driven pilot system for simulated chemical wastewater. **h** Purification performance of different catalytic systems for simulated chemical wastewater. **i** Removal of COD, NH_3-N, and TOC medical and coking wastewater by the pilot treatment unit. All error bars in the figure indicate the standard deviation from three replicate experiments. **j** Comparison of EE/O for different catalytic systems. **k** System boundaries for LCA analysis of CN-KI/PI/Vis system. **l** Sensitivity analysis of different stages in the CN-KI/PI/Vis system's lifecycle. **m** Comparison of carbon emissions of different catalytic systems.

The LCA[53] further quantified the environmental impact of the CN-KI/PI system throughout the water purification process, from catalyst preparation to pollutant degradation (Fig. 6k and Supplementary Fig. 80). Catalyst preparation and light source energy input stages exhibited relatively high environmental impacts, primarily due to the operation of high-power equipment. Sensitivity analysis pinpointed catalyst preparation as the dominant factor affecting the overall environmental pressure of the process (Fig. 6l and Supplementary Fig. 81). For future industrial applications, it is advisable to operate electrical equipment at full capacity and produce large batches of catalysts to minimize environmental impacts. The minor environmental impacted associated with light source energy input could be mitigated by adopting solar illumination. In practice, the developed outdoor pilot-scale reactor using the CN-KI/PI/Sunlight system significantly reduced all emission indicators. Carbon emissions for the CN-KI/PI system were substantially lower when compared with those for the Fenton, O_3, and H_2O_2/O_3 systems during the purification of the same wastewater, demonstrating its superior dynamic catalytic activity

(Fig. 6m, Supplementary Figs. 82–89 and Tables 33–39). During the purification of same wastewater, the carbon emissions for the Fenton, O_3, H_2O_2/O_3, and CN-KI/PI/Sunlight systems were 2.11×10^{-4} kg CO_2 eq L^{-1}, 0.120 kg CO_2 eq L^{-1}, 0.0721 kg CO_2 eq L^{-1}, and 0.137 kg CO_2 eq L^{-1}, respectively. This enhanced activity allowed the system to continuously treat at least 80 L of simulated chemical wastewater using free solar energy, further reducing its carbon footprint to 0.0376 kg CO_2 eq L^{-1}. Additionally, the CN-KI/PI/Sunlight system avoided the safety risks and subsequent costs associated with O_3 leakage and iron sludge precipitation and removal, positioning it as a preferred option for sustainable water purification technologies.

These detailed economic and environmental sustainability assessments confirmed the promising wastewater treatment potential of the CN-KI/PI system and provided strategic insights for future industrial-scale applications. By synthesizing large quantities of catalysts in a single batch, the long-term energy consumption of high-power equipment could be reduced. Furthermore, recycling the remaining PI in the catalytic system could enhance daily water treatment capacities and minimize environmental risks. Unreacted PI could also be adsorbed and reused to boost the photocatalytic activity of the CN substrate for superior H_2O_2 photosynthesis (Supplementary Fig. 90), aligning with global circular economy initiatives.

Discussion

In this work, we strived to design a "pre-catalyst", CN-KI, which features sites with interlayer constrained insertion, significantly enhancing light harvesting and exciton dissociation capabilities. The CN-KI/PI/Vis system demonstrated superior performance in purifying water contaminated with SMX, achieving almost complete removal within 5 min with a K value of 0.5681 min^{-1}, an order of magnitude higher than that of other reference systems. We further enhanced this system by dynamically reconstructing the pre-catalyst CN-KI during the photocatalytic reaction, introducing I^-/I_3^- redox mediators in-situ to create the "real catalyst", CN-KI-I_3. This catalyst exhibited enhanced intrinsic activity and could be recycled for at least 30 cycles, demonstrating progressively improved photocatalytic activity in the early cycles due to an increase in generated active species. Notably, the increase in dominant active species did not result from PI decomposition but rather from the functionalization of the reconstructed CN-KI-I_3 by PI, which enhanced the ORR process. The dynamic reconstruction of the pre-catalyst was comprehensively demonstrated through various analytical techniques, including theoretical calculations, *semi*-in-situ XPS, *semi*-in-situ CV, *semi*-in-situ i-t curves, and *semi*-in-situ UV-vis absorption spectra. The dynamic in-situ reconfiguration of CN-KI/PI system had demonstrated substantial industrial application potential for industrial applications, evidenced by its performance in both a continuous flow reactor and a pilot-scale reactor operating under natural sunlight. This system has shown impressive results in purifying real wastewater, as confirmed by evaluations including EE/O, and LCA assessments. Additionally, the CN-KI($-I_3$) catalyst showcased its versatility in applications beyond water purification, including photocatalytic production of H_2O_2. These findings highlight the potential use of CN-KI($-I_3$)/PI systems in wastewater treatment and provide valuable insights into the development of efficient CN-based or other-based photocatalysts through beneficial in-situ dynamic reconstruction.

Methods

Chemicals and reagents

Melamine (MA, AR), potassium iodide (KI, GR), sulfuric acid (H_2SO_4), sodium hydroxide (NaOH, 99%), periodate (PI, 98%), peracetic acid (PAA), hydrogen peroxide (H_2O_2), peroxymonosulfate (PMS), ethylenediaminetetraacetic acid disodium salt (EDTA-2Na), peroxydisulfate (PDS), *tert*-butyl alcohol (TBA), p-benzoquinone (p-BQ, AR), *L*-histidine, 2,2,6,6-tetramethyl-4-piperidinyl (TEMP), 5,5-dimethyl-1-pyrroline N-oxide (DMPO), N,N-diethyl-p-phenylenediamine (DPD), nitroblue tetrazolium (NBT, $C_{40}H_{30}N_{10}O_6C_{12}$), 1,3-diphylisobenzofuran ($C_{20}H_{14}O$, DPBF), sulfamethoxazole (SMX), sulfapyridine (SPY), bisphenol A (BPA), naproxen (NPX), ciprofloxacin (CIP), tetracycline (TC), sulfacetamide (SAM), rhodamine B (RhB), sodium carbonate anhydrous (Na_2CO_3), sodium bicarbonate ($NaHCO_3$), sodium chloride (NaCl), sodium sulfate anhydrous (Na_2SO_4), sodium dihydrogen phosphate anhydrous (NaH_2PO_4), sodium nitrate ($NaNO_3$), humic acid (HA), sodium thiosulfate ($Na_2S_2O_3$), isopropanol (IPA, AR), and acetonitrile were all purchased from Macklin Chemical Reagent Co., China, Sinopharm Chemical Reagent Co., China, Sigma-Aldrich Chemical Reagent Co., China or Shanghai Chemical Reagent Co., China. All solutions were prepared with deionized water with an 18.25 MΩ cm^{-1} resistivity.

Synthesis of photocatalysts

CN preparation. Melamine (2 g) was placed in a crucible with a lid and calcined in a tube furnace at 550 °C for 4 h, with a heating rate of 2.5 °C min^{-1}. The resultant product was then ground, washed, centrifuged ($12.58 \times 10^3 \times g$, 10 min), and dried, resulting in a material referred to as CN.

CN-KI preparation. Melamine and a specified potassium iodide (KI) were ultrasonically dissolved in 80 mL of deionized water. The solution was transferred to an oil bath and heated under stirring at 100 °C until dry, promoting recrystallization. The resultant white powder was then placed in a crucible with a lid and calcined in a tube furnace at 550 °C for 4 h, with a heating rate of 2.5 °C min^{-1}. After subsequent grinding, washing, centrifuging ($12.58 \times 10^3 \times g$, 10 min), and drying, the product was designated as CN-KI-X. The products were classified based on the copolymerized amount of KI into CN-KI-1 (Melamine: KI = 2:1 g), CN-KI-2 (Melamine: KI = 2:2 g), CN-KI-4 (Melamine: KI = 2:4 g), and CN-KI-5 (Melamine: KI = 2:5 g).

CN-KI-I_3 preparation. After undergoing a catalytic reaction, CN-KI was centrifuged ($12.58 \times 10^3 \times g$, 10 min), dried, and referred to as CN-KI-I_3.

Reaction system construction and catalytic performance evaluation

The photocatalytic performance of the samples for PI activation was evaluated by assessing the degradation of SMX at natural pH levels. For the experiments, 10 mg of the catalyst was ultrasonically dispersed in 50 mL of a 5 mg L^{-1} SMX aqueous solution. The mixture was then stirred in the dark for 5 min to achieve adsorption-desorption equilibrium. Illumination was provided by a 300 W xenon lamp equipped with a 420 nm cut-off filter, activated simultaneously with the addition of 1 mM PI to initiate the reaction. At predetermined intervals, 1 mL samples were extracted from the reaction mixture and immediately quenched with 100 µL of 100 mM sodium thiosulfate to halt further reaction. The samples were then centrifuged to separate the supernatant ($12.58 \times 10^3 \times g$, 15 min), which was subsequently analyzed to determine the remaining concentration of SMX. High-performance liquid chromatography-mass spectrometry (HPLC-MS, Agilent Co., USA) was utilized for this analysis (The flow phase details for monitoring various pollutants are provided in Supplementary Table 1).

Characterizations

XRD patterns of different as-prepared samples were obtained using a Bruker D8 Advance X-ray diffractometer (XRD) under Cu Kα X-ray radiation at 40 kV and 40 mA. Morphologies were characterized by Field Emission Scanning Electron Microscopy (FESEM, Apreo 2 C, Thermo Fisher Scientific Co., USA) and Transmission Electron Microscopy (TEM) with a FEI Tecnai 20 (Hitachi Co., Japan). UV-Vis Diffuse Reflectance Spectroscopy (UV-Vis DRS) was recorded on a UV3600-plus spectrophotometer (Shimadzu Co., Japan) spanning 200-800 nm. X-ray Photoelectron Spectroscopy (XPS) was identified using an

ESCALAB 250Xi spectrometer (Thermo Fisher Inc., USA). Surface areas of different samples were determined by the Brunauer-Emmett-Teller (BET) method using a Builder 4200 instrument (Tristar II 3020 M, Micromeritics Co., USA). Chemical groups of samples were identified by Fourier Transform Infrared Spectroscopy (FTIR, Nicolet Is10, Thermo Fisher Scientific Co., USA). Photoluminescence (PL) and time-resolved PL spectra were collected using an FLS-1000 fluorimeter. Dominant reactive active species in the system were reconfirmed using an ESR spectrometer (ER200-SRC, Bruker Co., USA) with various spin-trapping agents. Various photoelectrical properties of the samples were analyzed in a CHI660E electrochemical workstation. Total Organic Carbon (TOC) values were obtained on a TOC-VCPH analyzer (Multi N/C 2100, Analytic Jena AG, Germany). The chemical oxygen demand (COD) and ammonia nitrogen (NH_3-N) levels in real wastewater were measured using a UV-Vis spectrophotometer with colorimetric analysis. Ecological Structure-Activity Relationships (ECOSAR) system was used to evaluate the acute and chronic toxicity (CHV) of the original SMX and its degradation intermediates.

Density Functional Theory (DFT) calculations

The Perdew-Burke-Ernzerhof (PBE) functional was employed within the generalized gradient approximation framework for density functional theory (DFT) calculations[54]. A 2 × 1 × 1 k-point was used for geometry optimization. Plane-wave basis sets were used to represent valence electrons, with a kinetic energy cutoff of 400 eV. Partial occupancy of Kohn-Sham orbitals was introduced using the Gaussian smearing method with a width of 0.05 eV. Self-consistency in electronic energy calculations was ensured by setting the energy change criterion to less than 10^{-5} eV. Convergence was defined with an energy change limit of 0.02 eV/Ångström (eV $Å^{-1}$). A vacuum layer thickness of 20 Å was set to reduce artificial interactions between periodic images. Additionally, weak interactions were treated using DFT + D3 approach, implementing Grimme's empirical correction scheme. Furthermore, to gain insight into a more accurate understanding of the electronic structure of various systems in this investigation, the calculations were also performed using Heyd–Scuseria–Ernzerhof (HSE06) method.

In the designed catalytic system, the IO_4^- decomposition to produce $^1O_2$ was assumed to proceed through the following steps (Eqs. 6–9):

$$\textbf{Step}\,1: * + IO_4^- \rightarrow *IO_4^- \tag{6}$$

$$\textbf{Step}\,2: *IO_4^- + 2e^- \rightarrow *O + * IO_3^- \tag{7}$$

$$\textbf{Step}\,3: 2 * O + *IO_3^- \rightarrow *IO_3^- + *{}^1O_2 \tag{8}$$

$$\textbf{Step}\,4: *IO_3^- + *{}^1O_2 \rightarrow *IO_4^- + {}^1O_2 \tag{9}$$

The standard hydrogen electrode model was selected to calculate the free energy changes (ΔG) for each reaction pathway mentioned above[55,56]. $G(H^+)$ is typically described as $1/2\,G(H_2) - k_BT\ln(10) \times pH$ at non-zero pH ($p = 1$ bar, $T = 298.15\,K$). $\Delta G = \Delta E + \Delta ZPE - T\Delta S + \Delta G_U + \Delta G_{pH}$ is used to calculate the free energy for each step of the reaction, where ΔE, ΔZPE, and $T\Delta S$ represent the total energy, zero-point energy, and entropy contribution, respectively. In $\Delta G_U = -eU$, e is the elementary charge, and U is the electrode potential. ΔG_{pH} serves as the correction term for the free energy of H+. Additionally, the thermal stability of CN-KI and CN-KI-I_3 was evaluated using 20 ps of AIMD simulations at a controlled temperature of 373 K.

Toxicity analysis of SMX and its degradation products

The acute toxicity (LC_{50}), CHV, mutagenicity, bioaccumulation toxicity, and developmental toxicity of SMX and its degradation products were comprehensively predicted and assessed using the ECOSAR system and the T.E.S.T. The ECOSAR program, renowned for its robust ecological toxicity assessment capabilities, was employed to evaluate the toxicity levels of various intermediates towards aquatic organisms such as fish, water fleas, and green algae. These evaluations focused on acute toxicity (LC_{50}) and CHV metrics. Furthermore, detailed assessments of mutagenicity, bioaccumulation toxicity, and developmental toxicity for both the original SMX and its degradation products were conducted using the T.E.S.T system, which relied on quantitative structure-activity relationship (QSAR) principles. These comprehensive assessments provided valuable insights into the potential environmental impacts of SMX and transformation products.

Measurement of SMX and its intermediates

The concentration of SMX was detected on HPLC (1260 Infinity, Agilent Inc., USA) equipped with a UV detector and a ZORBAX SB C-18 column (5 μm, 4.6 × 250 mm). Acetonitrile and 0.1% formic acid water were used as the mobile phase (60:40, v/v), with a 1.0 mL min^{-1} flow rate. The detection wavelength was 259 nm, the injection volume was 20 μL, and the analysis time was 5 min. The degradation products of SMX were analyzed using a liquid chromatography-mass spectrometry (LC-MS) system comprising HPLC (6460, Agilent Inc., USA) with a Kromasil C18 column (4.6 × 250 mm) and an API 3000 mass spectrometer.

Measurements of other pollutant concentrations

The quantitative analysis of other organic pollutants in the broad-spectrum validation of the CN-KI/PI/Vis system followed the protocol outlined in "Measurement of SMX and its intermediates", with modifications to the mobile phase and detection wavelength only. Detailed parameters are specified in Supplementary Table 1.

Photoelectrochemical measurement

Transient photocurrent (*i-t*) responses, electrochemical impedance spectra, and MS curves were measured using a standard three-electrode system. A Pt plate and an Ag/AgCl electrode were used as the counter and reference electrodes, respectively. A mixture comprising 5 mg of catalyst, 2 mL of ethanol, and 20 μL of Nafion solution was coated onto FTO glass to prepare the working electrode. A 0.1 M Na_2SO_4 aqueous solution served as the electrolyte, with data recorded by a CHI 760E electrochemical workstation (Chenhua Instrument Co., China).

Semi-in-situ i-t testing

The procedure for obtaining *semi*-in-situ transient *i-t* curves adhered to the methods is detailed in "Photoelectrochemical measurement", with the sole modification being the replacement of the working electrode.

Semi-in-situ CV testing

The process for obtaining *semi*-in-situ CV curves followed the guidelines in "Photoelectrochemical measurement", necessitating changes to different working electrodes and using pure water as the electrolyte.

Semi-in-situ UV-visible absorption spectroscopy

Semi-in-situ UV-visible absorption spectroscopy was performed on a UV-vis spectrophotometer (TU-1901). Specifically, a specific amount of CN-KI sample was ultrasonically dispersed in 50 mL of deionized water, and the light source was turned on, simulating the degradation process of organic pollutants in the CN-KI/PI/Vis system. The mixed solution was collected and centrifuged ($12.58 \times 10^3 \times g$, 10 min) at different light exposure times, the supernatant was taken, and a full spectrum scan was performed on the TU-1901. The wavelength range was 200–500 nm, and the scanning interval was 1 nm.

PI concentration measurement

The concentration of PI was determined by the DPD colorimetric method. Specifically, a certain volume of deionized water was adjusted to a pH of 3.0 and aerated with N_2 for 30 min as solution A. A 40 mM $FeSO_4$ solution was prepared using solution A as solution B. A 100 mM DPD solution was prepared using solution A as solution C. The solution to be tested, after centrifugation ($12.58 \times 10^3 \times g$, 10 min) as solution D. In a colorimetric tube, 1 mL of solution B, 0.4 mL of solution C, and 0.2 mL of solution D were combined. The volume was then adjusted to 10 mL with solution A. The absorbance of the mixture was measured at 510 nm using a UV-visible spectrophotometer to determine the PI concentration.

Quantify the concentrations of ROS

Nitroblue tetrazolium (NBT) and 1,3-diphenylisobenzofuran (DPBF) were used as probes to detect superoxide radicals ($^{\cdot}O_2^-$) and ($^1O_2$), respectively. The photocatalytic reaction was initiated after adding specific amounts of these probes along with CN-KI to the solution. Sample collection was conducted similarly to the catalytic degradation experiments. To quantify the concentrations of NBT and DPBF, absorbance readings were taken at 259 nm for NBT and 410 nm for DPBF using a UV-vis spectrophotometer. The concentrations of $^{\cdot}O_2^-$ (4:1) and $^1O_2$ (1:1) were calculated based on their stoichiometric reaction ratios with the corresponding probes.

Calculation of PI apparent quantum yield

Considering the critical role of oxidant quantum yield in determining the concentration of produced radicals, the quantum yield of PI under 400 nm excitation was calculated using the following formula[46,57,58].

$$\Phi_{PI} = 10 \times K \times U_\lambda / (Ln10 \times \varepsilon_{PI}) \quad (10)$$

$$U_\lambda = h \times c \times NA / \lambda \quad (11)$$

$$K = [Ln(C_0/C_t)]/E_0 \times t \quad (12)$$

In the formula, Φ represents the calculated apparent quantum yield of PI (mol Einstein^{-1}), U_λ is the molar photon energy (J Einstein^{-1}), K is the flux-based photolysis rate constant of PI (cm^2 mJ^{-1}), ε_{PI} is the molar absorption coefficient of PI at a specific wavelength (M^{-1} cm^{-1}, $\lambda = 400$ nm, $\varepsilon = 490$ M^{-1} cm^{-1})[57], h is Planck constant (6.626×10^{-34} J s), c is the speed of light (3×10^8 m × s^{-1}), NA is Avogadro constant (6.022×10^{23} mol^{-1}), λ is the wavelength (m, 400×10^{-9} m), E_0 is the fluence rate (mW cm^{-2}, 8.73 mW cm^{-2}), C_0 and C_t represent the concentration of PI at time 0 and time t, respectively, and t is the reaction time. Based on the photolysis kinetics of PI and the relevant parameters (Supplementary Fig. 56), the quantum yield (Φ_{PI}) of PI at 400 ± 5 nm in this study was calculated to be 0.363 mol Einstein^{-1}.

Catalyst loading

To design a floating catalyst, CN-KI was immobilized onto a hydrophobic sponge. Briefly, a mixture was prepared using 300 mg of catalyst, 50 mL of ethanol, and 200 µL of Nafion solution. The mixture was then applied to the pre-prepared hydrophobic sponge and dried in an oven at 60 °C for future use.

Solar panel reactor design

Two solar panel reactors, tailored for different applications, were independently developed. A smaller reactor, with an effective area of 25 cm^2, was specifically designed for continuous degradation experiments within the laboratory setting. In contrast, the larger reactor, which boasts an effective area of 1 m^2 (and 900 cm^2), was created for outdoor experiments utilizing natural sunlight. Both reactors comprised three main components: a cover plate, a gasket, and a base plate equipped with U-shaped grooves that serve as water channels. Catalytic pathways were ingeniously created by embedding sponges, which were loaded with the catalyst, into these pre-designed grooves. The flow rate by these catalytic pathways was controlled by a peristaltic pump. Depending on the experimental setting, the light source was either a xenon lamp for indoor experiments or natural sunlight for the outdoor setup. In dynamic degradation experiments, target pollutants and oxidant mixtures were continuously passed through these catalytic pathways. Reactor effluents were collected for analysis at predetermined time intervals, and pollutant concentrations and TOC were measured to assess the catalytic performance.

Pilot-scale reactor setup

The independently developed pilot-scale reactor system consisted of a water tank, a stirrer, and a floating catalyst. The system was used to evaluate the purification efficiency of simulated chemicals, real coking, and real medical wastewaters under sunlight to assess its industrial applicability.

The reactor was filled with 20 L of wastewater for purification. The design of the floating catalyst could effectively alleviate the problems associated with light penetration and catalyst recovery in practical photocatalytic applications. The purification process was carried out under direct natural sunlight (Chongqing City, China). Throughout the process, samples were taken at intervals to analyze pollutant removal efficiency and to assess key indicators such as COD, NH_3-N, TOC, chromaticity, and salinity. This approach provides a comprehensive assessment of reactor performance under real-world conditions.

Cost analysis

An economic evaluation was conducted to assess the potential for practical application of the CN-KI-PI system in different treatment scenarios using the concept of Electrical Energy per Order (EE/O), which was defined as the amount of energy required to achieve first-order pollutant removal. EE/O is defined as the energy required to achieve first-order pollutant removal. In the CN-KI-PI system, EE/O included the costs of catalyst preparation, PI input, and energy consumption during the degradation process[51,52,59].

The cost of catalyst preparation can be calculated using the following formula:

$$Catalyst/O = \alpha C_{Catalyst} / \log(C_0/C_t) \quad (13)$$

Where α is a unit conversion factor that converts the catalyst amount to energy units (7.928 kWh g^{-1} for CN-KI, 3.7×10^{-3} kWh g^{-1} for Fe^{2+}), $C_{Catalyst}$ is the catalyst concentration (0.2 g L^{-1} for indoor, 0.00375 g L^{-1} for outdoor experiments), $\log(C_0/C_t)$ represents the pollutant removal level, set to a value of 10 for these calculations.

The cost of oxidant input can be calculated using the following formula:

$$Oxidant/O = \beta C_{Oxidant} / \log(C_0/C_t) \quad (14)$$

Where β is the unit conversion factor that converts the oxidant amount to energy units (12.5×10^{-3} kWh g^{-1} for PI, 9.42×10^{-3} kWh g^{-1} for H_2O_2), $C_{Oxidant}$ is the oxidant concentration (0.214 g L^{-1} for PI indoors, 1.67×10^{-3} g L^{-1} for PI outdoors, 0.018 g L^{-1} for H_2O_2).

The energy input during the degradation process can be calculated using the following formula:

$$EE/O_{Light} = P \times t/V \times \log(C_0/C_t) \quad (15)$$

Where P is the input energy of the xenon lamp (kWh min^{-1}), t is the reaction time (min), V is the treatment volume (L).

To compare the energy consumption of the CN-KI-PI system with reported systems on a larger scale, P is defined as the input power of

the light source (kW), and $\log(C_0/C_t)$ is converted to $0.4343K_{obs}$×t. The equation can then be rewritten as:

$$EE/O_{Light-1} = P_1 \times t/60 \times V \times 0.4343K_{obs} \times t = P_1/(26.058V \times K_{obs}) \quad (16)$$

Where P_1 is the input power of the xenon lamp (kW), V is the treatment volume (L), K_{obs} is the first-order rate constant.

Life Cycle Assessment (LCA) analysis

A LCA was performed to thoroughly quantify the significant environmental impacts associated with scaling up the CN-KI/PI system[53,60]. This analysis utilized data derived from both laboratory and outdoor scale experiments to define functional units for each treatment system. Simapro software (version 9.0) and the Ecoinvent database were used for inventory modeling of the lifecycle environmental impacts. The system boundaries for each purification system are referenced in Supplementary Fig. 79, with critical parameters outlined in Supplementary Tables 33–39. The assessment applied a prescriptive evaluation method and enhanced the robustness of the findings through the execution of 1000 Monte Carlo simulations, aiming to quantify the uncertainty associated with the estimated environmental impacts. A total of 18 impact categories were selected. These included five categories related to the atmospheric effects: (1) GWP (kg CO_2 equivalent), (2) SOD (kg CFC-11 equivalent), (3) IR (kBq Co-60 equivalent), (4) OFHH (kg NO_x equivalent), and (5) FPM (kg PM2.5 equivalent). The terrestrial ecosystem impact categories were divided into three types: (6) OFTE (kg NO_x equivalent), (7) TA (kg SO_2 equivalent), and (8) TE (kg 1,4-dcb equivalent). There were two categories focusing on human health: (13) HCT (kg 1,4-dcb per kg) and (14) HNT (kg 1,4-dcb per kg). Additionally, four categories address resource depletion: (15) LU (m^2a crop equivalent), (16) MRS (kg Cu equivalent), (17) FRS (kg oil equivalent), and (18) WC (m^3). The results of the LCA were normalized to enable a coherent comparison of environmental impacts across different treatment systems.

E. coli cultivation

The survival density of *E. coli* (BL21, wild bacteria) was investigated to evaluate the toxicity effects of different catalytic systems on the degradation intermediates. Specifically, an equal volume of *E. coli* stock solution was inoculated into fresh LB medium and cultured for 10 h in a shaking incubator (37 °C) to obtain activated bacterial populations (first generation). Experimental group LB media were prepared using water samples detoxified by different catalytic systems, while control group LB media were prepared using LB medium with original SMX and deionized water. An equal volume of the obtained first-generation bacterial population was inoculated into the different LB media and cultured under the same conditions for 8 h. Afterward, 100 μL of the cultures (diluted 1000-fold) were inoculated onto agar plates and incubated at 37 °C for 18 h. The survival density of *E. coli* was determined using the plate counting method. Each experiment was repeated three times to reduce experimental errors. The survival rate of bacteria was calculated using the formula:

$$\text{Survival rate} = (M/N) \times 100\% \quad (17)$$

where M represents the colony count obtained from the experimental group, and N represents the colony count received from the deionized water control group. All experiments were conducted in a laminar flow hood, and disposable materials were sterilized using an autoclave.

Zebrafish embryo cultivation

The bio-toxicity of degradation intermediates from various catalytic systems was evaluated using Zebrafish embryo hatching as an indicator. Specifically, water samples treated by different catalytic systems served as exposure solutions, with untreated SMX and a nutrient solution (Blank) as control groups. Robust embryos at the 8-cell stage were obtained and placed in cell culture plates, each receiving 1 mL of the exposure solution and 1 mL of nutrient solution. The development of the embryos was meticulously observed and documented under a microscope every 24 h. This monitoring continued until hatching occurred in the Blank group. To ensure reliability and minimize experimental errors, each experiment was conducted five times.

Wheat growth experiments

The germination of wheat seeds was employed to assess the phytotoxicity of degradation intermediates from various catalytic systems. Water samples treated by different catalytic methods were used as irrigation sources, with untreated SMX and deionized water serving as control groups. Twenty robust wheat seeds were evenly placed at the bottom of culture dishes lined with filter paper. Each dish received 5 mL of the respective water samples to support seed germination and growth.

Photographs were taken at 24-h intervals to document the progress of wheat growth. The water in each dish was replenished as it was consumed. After 168 h, the lengths of roots and shoots were measured to evaluate the growth performance of the wheat under treatment conditions.

H_2O_2 photocatalytic production

H_2O_2 artificial photosynthesis was explored to further assess the scalable application models of the CN-KI catalyst featuring in-situ restructuring capabilities. Briefly, 5 mg of the catalyst was dispersed in 10 mL of deionized water with 10% isopropanol using ultrasonication. The mixture was stirred in the dark for 10 min to ensure adsorption-desorption equilibrium. The photocatalytic reaction was conducted under xenon lamp illumination with a cutoff filter of $\lambda \geq 420$ nm. Samples were collected every 10 min, and the concentration of H_2O_2 was determined using the potassium titanyl oxalate method.

Assessment of the optical properties of the obtained photocatalysts

The optical properties of catalysts are crucial for understanding their photon absorption and photocatalytic activity, which is essential for evaluating the performance of light-assisted oxidant activation. One indicator of optical performance is the positive correlation between optical thickness and catalyst concentration, as shown in Supplementary Table 40. Simulations using the six-flux model suggest that the optimal optical thickness for the designed reaction system should be between 1.8 and 4.4. Calculations incorporating corresponding reaction parameters indicate that the catalyst concentration should be maintained within 0.2 to 0.3 g L^{-1} to achieve optimal optical thickness (Eqs. 18–22), aligning with our parameter optimization experiments (Supplementary Fig. 9). This observation confirms the reliability of our parameter optimization results and indicates that maintaining catalyst concentration within a reasonable range is necessary to enhance the efficiency of the light-assisted catalyst activation of the oxidant.

$$\kappa^* = \frac{\int_{\lambda min}^{\lambda max} \kappa_\lambda^* I_\lambda d\lambda}{\int_{\lambda min}^{\lambda max} I_\lambda d\lambda} \quad (18)$$

$$\sigma^* = \frac{\int_{\lambda \min}^{\lambda \max} \sigma_\lambda^* I_\lambda d\lambda}{\int_{\lambda \min}^{\lambda \max} I_\lambda d\lambda} \quad (19)$$

$$\tau = (\sigma^* + \kappa^*) C_{cat} L \quad (20)$$

$$\beta^* = \sigma^* + \kappa^* \quad (21)$$

where C_{cat} is the photocatalyst loading, σ^* and κ^* are the spectral average specific scattering and absorption coefficients, respectively, and L is the characteristic length of light extinction in the reactor, which is 80 mm. The obtained scattering coefficient (σ^*), absorption coefficient (κ^*), and extinction coefficient (β^*) are listed in Supplementary Table 40.

The optical thickness of different materials could be calculated as follows:

$$\tau_{app} = a\tau\sqrt{1-\omega_{corr}^2} \tag{22}$$

The quantification of the Local Volumetric Rate of Photon Absorption (LVRPA) is employed to understand the photon absorption kinetics within the light-assisted oxidant activation system (Eqs. 23–28). As depicted in Supplementary Fig. 90, there is a positive correlation between the catalyst concentration and its surface LVRPA. The CN-KI shows a higher slope compared to CN, indicating superior photon absorption capability and enhanced photocatalytic properties (Supplementary Fig. 70 and Supplementary Table 41). This study underscores the importance of photocatalyst optical properties and the selection of appropriate reaction conditions for improving the photocatalytic performance of the designed system, providing theoretical support for the development of efficient and sustainable photocatalytic reaction systems.

$$LVRPA = \frac{I_0\tau_{app}}{\omega_{corr}(1-\gamma)L}\left[(\omega_{corr}-1+\sqrt{1-\omega_{corr}^2})e^{-\frac{x\tau_{app}}{L}}+\gamma(\omega_{corr}-1-\sqrt{1-\omega_{corr}^2})e^{\frac{x\tau_{app}}{L}}\right] \tag{23}$$

Among a, b, ω_{corr}, and γ are defined below:

$$a = 1-\omega p_f-\frac{4\omega^2 p_s^2}{1-\omega p_f-\omega p_b-2\omega p_s} \tag{24}$$

$$b = \omega p_b+\frac{4\omega^2 p_s^2}{1-\omega p_f-\omega p_b-2\omega p_s} \tag{25}$$

$$\omega_{corr} = b/a \tag{26}$$

$$\gamma = \frac{1-\sqrt{1-\omega_{corr}^2}}{1+\sqrt{1-\omega_{corr}^2}}e^{-2\tau_{app}} \tag{27}$$

$$TRPA = \int_0^L LVRPA\,dx \tag{28}$$

Reporting summary

Further information on research design is available in the Nature Portfolio Reporting Summary linked to this article.

Data availability

The data generated in this study are provided in the Supplementary Information/Source Data file. All data underlying this study are available from the corresponding author upon request. Source data are provided with this paper.

References

1. Chen, F. et al. Single-atom iron anchored tubular g-C_3N_4 catalysts for ultrafast fenton-like reaction: roles of high-valency iron-oxo species and organic radicals. *Adv. Mater.* **34**, 2202891 (2022).
2. Wang, A. W. et al. Enhanced and synergistic catalytic activation by photoexcitation driven S– scheme heterojunction hydrogel interface electric field. *Nat. Commun.* **14**, 6733 (2023).
3. Lian, Z. C. et al. Photo-self-Fenton reaction mediated by atomically dispersed Ag-Co photocatalysts toward efficient degradation of organic pollutants. *Angew Chem. Int. Ed.* **63**, e202318927 (2024).
4. Wu, X. L. et al. Directional and ultrafast charge transfer in oxygen-vacancy-rich ZnO@ single-atom cobalt core-shell junction for photo-Fenton-like reaction. *Angew Chem. Int. Ed.* **135**, e202305639 (2023).
5. Xiong, L. Q. & Tang, J. W. Strategies and challenges on selectivity of photocatalytic oxidation of organic substances. *Adv. Energy Mater.* **11**, 2003216 (2021).
6. Yang, J. L., Zhu, M. S. & Dionysiou, D. D. What is the role of light in persulfate-based advanced oxidation for water treatment? *Water Res.* **189**, 116627 (2021).
7. Cao, S. W., Low, J. X., Yu, J. G. & Jaroniec, M. Polymeric photocatalysts based on graphitic carbon nitride. *Adv. Mater.* **27**, 2150–2176 (2015).
8. Zhang, G. G., Lan, Z. A. & Wang, X. C. Conjugated polymers: catalysts for photocatalytic hydrogen evolution. *Angew Chem. Int. Ed.* **55**, 15712–15727 (2016).
9. Godin, R., Wang, Y. O., Zwijnenburg, M. A., Tang, J. W. & Durrant, J. R. Time-resolved spectroscopic investigation of charge trapping in carbon nitrides photocatalysts for hydrogen generation. *J. Am. Chem. Soc.* **139**, 5216–5224 (2017).
10. Tang, C. S. et al. Recent progress in the applications of non-metal modified graphitic carbon nitride in photocatalysis. *Coord. Chem. Rev.* **474**, 214846 (2023).
11. Wang, Q. et al. Bottom-up synthesis of single-crystalline poly (Triazine Imide) nanosheets for photocatalytic overall water splitting. *Angew Chem. Int. Ed.* **135**, e202307930 (2023).
12. Xue, C. et al. Simultaneous organic pollutant degradation and hydrogen peroxide production by molecular-engineered carbon nitride. *Appl. Catal. B Environ.* **340**, 123259 (2024).
13. He, F. T. et al. Rejoint of carbon nitride fragments into multi-interfacial order-disorder homojunction for robust photo-driven generation of H_2O_2. *Adv. Mater.* **36**, 2307490 (2024).
14. Wang, Y. O., Godin, R., Durrant, J. R. & Tang, J. W. Efficient hole trapping in carbon dot/oxygen-modified carbon nitride heterojunction photocatalysts for enhanced methanol production from CO_2 under neutral conditions. *Angew Chem. Int. Ed.* **60**, 20811–20816 (2021).
15. Lin, J. K. et al. Functional carbon nitride materials in photo-Fenton-like catalysis for environmental remediation. *Adv. Funct. Mater.* **32**, 2201743 (2022).
16. Wang, Z. W. et al. Cobalt single atoms anchored on oxygen-doped tubular carbon nitride for efficient peroxymonosulfate activation: simultaneous coordination structure and morphology modulation. *Angew. Chem. Int. Ed.* **61**, e202202338 (2022).
17. Teng, Z. et al. Atomically dispersed low-valent Au boosts photocatalytic hydroxyl radical production. *Nat. Chem.* **16**, 1250–1260 (2024).
18. Zhao, Y. et al. Mechanistic analysis of multiple processes controlling solar-driven H_2O_2 synthesis using engineered polymeric carbon nitride. *Nat. Commun.* **12**, 3701 (2021).
19. Cheng, J. J. et al. Metalized carbon nitrides for efficient catalytic functionalization of CO_2. *ACS Catal* **12**, 1797–1808 (2022).
20. Wu, S., Yu, H. T., Chen, S. & Quan, X. Enhanced photocatalytic H_2O_2 production over carbon nitride by doping and defect engineering. *ACS Catal.* **10**, 14380–14389 (2020).
21. Xu, Y. S. et al. Homogeneous carbon/potassium-incorporation strategy for synthesizing red polymeric carbon nitride capable of near-infrared photocatalytic H_2 production. *Adv. Mater.* **33**, 2101455 (2021).

22. Guo, S. E. et al. Phosphorus-doped carbon nitride tubes with a layered micro-nanostructure for enhanced visible-light photocatalytic hydrogen evolution. *Angew Chem. Int. Ed.* **55**, 1830–1834 (2016).
23. Liu, W. et al. Unraveling the mechanism on ultrahigh efficiency photocatalytic H_2O_2 generation for dual-heteroatom incorporated polymeric carbon nitride. *Adv. Funct. Mater.* **32**, 2205119 (2022).
24. Xiao, X. D. et al. A promoted charge separation/transfer system from Cu single atoms and C_3N_4 layers for efficient photocatalysis. *Adv. Mater.* **33**, 2003082 (2020).
25. Kuang et al. Ultrastable low-bias water splitting photoanodes via photocorrosion inhibition and in situ catalyst regeneration. *Nat. Energy* **2**, 16191 (2017).
26. Liu, Y. X. et al. Cu_2O/2D COFs core/shell nanocubes with anti-photocorrosion ability for efficient photocatalytic hydrogen evolution. *ACS Nano* **17**, 5994–6001 (2023).
27. Gao, R. T. et al. Dynamic semiconductor-electrolyte interface for sustainable solar water splitting over 600 hours under neutral conditions. *Sci. Adv.* **9**, 4589 (2023).
28. Zhao, S. L. et al. Structural transformation of highly active metal-organic framework electrocatalysts during the oxygen evolution reaction. *Nat. Energy* **5**, 881–890 (2020).
29. Yao, N. et al. Intermolecular energy gap-induced formation of high-valent cobalt species in CoOOH surface layer on cobalt sulfides for efficient water oxidation. *Appl. Catal. B-Environ.* **61**, e202117178 (2022).
30. Wang, J. Controlling dynamic reconstruction chemistry for superior oxygen-evolving catalysts. *Chem-Us* **9**, 1645–1657 (2023).
31. Zhang, Y. Q. et al. Rapid synthesis of cobalt nitride nanowires: highly efficient and low-cost catalysts for oxygen evolution. *Angew Chem. Int. Ed.* **55**, 8670–8674 (2016).
32. Minguzzi, A. How to improve the lifetime of an electrocatalyst. *Nat. Catal.* **3**, 687–689 (2020).
33. Peng, L. S. et al. Atomic cation-vacancy engineering of NiFe-layered double hydroxides for improved activity and stability towards the oxygen evolution reaction. *Angew Chem. Int. Ed.* **60**, 24612 (2021).
34. Kang, J. X. et al. Valence oscillation and dynamic active sites in monolayer NiCo hydroxides for water oxidation. *Nat. Catal.* **4**, 1050–1058 (2021).
35. Zhang, T. S. et al. Redox mediator chemistry regulated aqueous batteries: insights into mechanisms and prospects. *CCS Chem* **4**, 2874–2887 (2022).
36. Lei, J. F., Yao, Y. X., Wang, Z. Y. & Lu, Y. C. Towards high-areal-capacity aqueous zinc-manganese batteries: promoting MnO_2 dissolution by redox mediators. *Energy Environ. Sci.* **14**, 4418–4426 (2021).
37. Cui, M. W. et al. I_3^-/I^- Redox Reaction-mediated Organic Zinc-Air Batteries with Accelerated Kinetics and Long Shelf Lives. *Angew. Chem. Int. Ed* **62**, e202303845 (2023).
38. Li, D. F. et al. Ru(III)-periodate for high performance and selective degradation of aqueous organic pollutants: important role of Ru(V) and Ru(IV). *Environ. Sci. Technol.* **57**, 12094–12104 (2023).
39. Zong, Y. et al. Enhanced oxidation of organic contaminants by iron (II)-activated periodate: the significance of high-valent iron-oxo species. *Environ. Sci. Technol.* **55**, 7634–7642 (2021).
40. Chen, F. et al. Embedding electronic perpetual motion into single-atom catalysts for persistent Fenton-like reactions. *Proc. Natl. Acad. Sci. USA* **121**, e2314396121 (2024).
41. Zhang, G. G. et al. Electron deficient monomers optimizes nucleation and enhances photocatalytic redox activity of carbon nitrides. *Angew. Chem. Int. Ed.* **58**, 14950–14954 (2019).
42. Ong, W. J., Tan, L. L., Ng, Y. H., Yong, S. T. & Chai, S. P. Graphitic carbon nitride (g-C_3N_4)-based photocatalysts for artificial photosynthesis and environmental remediation: are we a step closer to achieving sustainability? *Chem. Rev.* **116**, 7159–7329 (2016).
43. Zhang, G. Q., Xu, Y. S., He, C. X., Zhang, P. X. & Mi, H. W. Oxygen-doped crystalline carbon nitride with greatly extended visible-light-responsive range for photocatalytic H_2 generation. *Appl. Catal. B-Environ.* **283**, 119636 (2021).
44. Li, F. et al. Understanding the unique S-scheme charge migration in triazine/heptazine crystalline carbon nitride homojunction. *Nat. Commun.* **14**, 3901 (2023).
45. Su, L. N., Wang, P. F., Ma, X. L., Wang, J. H. & Zhan, S. H. Regulating local electron density of iron single sites by introducing nitrogen vacancies for efficient photo-Fenton process. *Angew. Chem. Int. Ed.* **60**, 21261 (2021).
46. Chen, L. et al. Solar-light-activated periodate for degradation and detoxification of highly toxic 6PPD-quinone at environmental levels. *Nat. Water.* **2**, 453–463 (2024).
47. Sun, H., He, F. & Choi, W. Production of reactive oxygen species by the reaction of periodate and hydroxylamine for rapid removal of organic pollutants and waterborne bacteria. *Environ. Sci. Technol.* **54**, 6427–6437 (2020).
48. Chen, T. et al. Understanding the importance of periodate species in the pH-dependent degradation of organic contaminants in the H_2O_2/periodate process. *Environ. Sci. Technol.* **56**, 10372–10380 (2022).
49. Niu, L. et al. Ferrate (VI)/periodate system: synergistic and rapid oxidation of micropollutants via periodate/iodate-modulated Fe(IV)/Fe(V) intermediates. *Environ. Sci. Technol.* **57**, 7051–7062 (2023).
50. Chen, X. J. et al. pH-driven efficacy of the ferrate (VI)-peracetic acid system in swift sulfonamide antibiotic degradation: a deep dive into active species evolution and mechanistic insights. *Environ. Sci. Technol.* **57**, 20206–20218 (2023).
51. Mao, Y., Yu, B., Wang, P., Yue, S. & Zhan, S. Efficient reduction-oxidation coupling degradation of nitroaromatic compounds in continuous flow processes. *Nat. Commun.* **15**, 6364 (2024).
52. Cater, S. R., Stefan, M. I., Bolton, J. R. & Safarzadeh-Amiri, A. UV/H_2O_2 treatment of methyl tert-butyl ether in contaminated waters. *Environ. Sci. Technol.* **34**, 659–662 (2000).
53. Zhang, G. et al. Ammonia recovery from nitrate-rich wastewater using a membrane-free electrochemical system. *Nat. Sustain.* **7**, 1251–1263 (2024).
54. Perdew, J. P. et al. Generalized gradient approximation for the exchange-correlation hole of a many-electron system. *Phys. Rev. B.* **54**, 16533 (1996).
55. Jiao, Y., Zheng, Y., Jaroniec, M. & Qiao, S. Z. Origin of the electrocatalytic oxygen reduction activity of graphene-based catalysts: a roadmap to achieve the best performance. *J. Am. Chem. Soc.* **136**, 4394–4403 (2014).
56. Nørskov, J. K. et al. Origin of the overpotential for oxygen reduction at a fuel-cell cathode. *J. Phys. Chem. B.* **108**, 17886–17892 (2004).
57. Li, J. et al. Ozone-and hydroxyl radical-induced degradation of micropollutants in a novel UVA-LED-activated periodate advanced oxidation process. *Environ. Sci. Technol.* **57**, 18607–18616 (2023).
58. Yang, T. et al. UVA-LED-assisted activation of the ferrate (VI) process for enhanced micropollutant degradation: important role of ferrate (IV) and ferrate (V). *Environ. Sci. Technol.* **56**, 1221–1232 (2021).
59. Zhang, R., Yang, Y., Huang, C.-H., Zhao, L. & Sun, P. Kinetics and modeling of sulfonamide antibiotic degradation in wastewater and human urine by UV/H_2O_2 and UV/PDS. *Water Res* **103**, 283–292 (2016).
60. Wu, Z. et al. Long-range interactions driving neighboring Fe-N_4 sites in Fenton-like reactions for sustainable water decontamination. *Nat. Commun.* **15**, 7775 (2024).

Acknowledgements

The authors thank the National Natural Science Foundation of China (Nos. 52270149, 51908528, 52192684, and 51821006) and the Fundamental Research Funds for the Central Universities (Nos. 2024IAIS-

QN013, 2021CDJQY-014) for supporting this work. The authors also thank the related testers from Shiyanjia Lab (www.shiyanjia.com) for the measurements. We would like to thank Analytical and Testing Center of Chongqing University for LC-MS measurements.

Author contributions

F.C. and C.B. conceived and planned the experiments, and C.B. and F.Y. conducted the related experiments. P.D. contributed to the DFT calculations. C.B. and F.Y. conducted, and Z.Z., Y.S., X.C., P.D., and F.C. assisted in collecting data and analyzing various characterizations. C.B., F.C., and H.Y. wrote and revised the manuscript.

Competing interests

The authors declare no competing interests.

Additional information

Supplementary information The online version contains supplementary material available at https://doi.org/10.1038/s41467-025-58392-3.

Correspondence and requests for materials should be addressed to Fei Chen or Han-Qing Yu.

Peer review information *Nature Communications* thanks Youyong Li, Jiahai Ma and the other, anonymous, reviewer(s) for their contribution to the peer review of this work. A peer review file is available.